Granular Matter (2026) 28:60
https://doi.org/10.1007/s10035-026-01646-8

RESEARCH

Super-time-stepping acceleration within the discrete element framework for thermal and electric analyses in granular materials

Jerzy Rojek[1] · **Fatima Nisar**[1]

Received: 28 November 2025 / Accepted: 20 April 2026

Abstract

Heat transfer and electrical transport in granular materials are important phenomena in many engineering applications. The discrete element method (DEM) is commonly used to simulate conduction in such media. The DEM usually employs explicit time integration algorithms due to their computational efficiency. The first-order differential equations describing transient thermal or electric problems in the DEM are commonly solved using the forward Euler explicit solution scheme. All explicit schemes have a serious disadvantage of conditional stability, which limits the time step length. The present paper introduces the super-time-stepping (STS) acceleration method into the DEM framework for transient thermal and electric problems governed by the first-order differential equations. The STS idea consists of relaxing the stability condition for single steps and imposing the stability on a cycle of steps (substeps), making up the so-called superstep. The length of the superstep is much longer than the critical time step of the standard explicit time integration. This is an established method for solving parabolic differential equations, commonly recognized for its advantages over the standard explicit time integration. Despite the efficiency, its application within the DEM framework remains unexplored. Herein, STS is applied to thermal and thermoelectric simulations. The efficiency and accuracy of the STS scheme for different combinations of parameters are investigated. The results demonstrate that speedup of up to 15 is achievable without compromising accuracy. The strong performance justifies a wider applicability of the STS acceleration scheme in the DEM for problems governed by the first-order differential equations.

Keywords Granular materials · Thermal · Electric · Discrete element method · Explicit time integration · Super-time-stepping acceleration

1 Introduction

Heat transfer and current flow in granular materials are important phenomena in many engineering applications. Heat conduction is crucial in applications such as thermal insulation [1], powder metallurgy, 3D printing [2], combustion reactors [3], and fluidized beds [4]. Conversely, electrical properties are essential, for instance, in batteries [5], granular metal films [6, 7], and tactile sensing devices [8]. Furthermore, applications like thermoelectric systems [9] and electric-current assisted sintering [10] rely on the interplay of both thermal and electrical phenomena. Our research is mainly motivated by the electric-current-assisted sintering, but the developments are general and relevant to any applications of electric current flow and heat transfer in granular materials.

The behaviour of granular materials is highly complex, as thermal and electrical conduction not only depend on the bulk transport properties of the grains themselves but also on the microstructure of the granular materials and the intergranular transport mechanisms. Numerical analysis is indispensable for understanding the behaviour of granular materials and determining effective transport properties. The discrete element method (DEM) is a typical tool for simulating heat and electrical transport in granular materials, e.g. [11, 12]. The main drawback of the DEM is the conditional stability of the explicit solution scheme usually employed in the DEM, which limits the time step. The present paper

✉ Fatima Nisar
fnisar@ippt.pan.pl

Jerzy Rojek
jrojek@ippt.pan.pl

[1] Institute of Fundamental Technological Research, Polish Academy of Sciences, Pawińskiego, 02-106 Warsaw, Poland

Published online: 21 May 2026

presents a possibility to improve the efficiency of thermal and electrical simulations with the DEM by the so-called super-time-stepping acceleration algorithm, which enables us to use larger time steps.

The discrete element method was first introduced to simulate the dynamics of granular materials [13, 14]. It was successfully applied to model cohesive materials such as rocks, e.g. [15–17]. It was further extended to model thermal problems, e.g. [18, 19], as well as electrical problems, e.g. [12, 20, 21]. Transient thermal problems in the DEM framework can be solved by any explicit or implicit scheme. Zohdi [20] used an iterative implicit scheme for time integration of the thermal problem in the framework of the thermo-electro-mechanical model of electrically enhanced sintering of powdered materials. Zhang et al. [22] performed the time discretisation using an implicit finite difference scheme, the generalised trapezoidal method, also known as the generalised midpoint rule.

However, explicit time integration methods, such as the forward Euler method, due to their compatibility with the standard formulation of the DEM and computational efficiency, are commonly chosen to solve the thermal equations in the DEM, especially for coupled thermomechanical problems, as it was pointed out by Feng et al. [18]. Particle temperatures are computed in an explicit manner using forward Euler integration in a thermomechanical DEM model of granular flow by [23]. The explicit forward Euler scheme was used by Terreros et al. [24] in the time integration of the thermal part of the thermomechanical model of friction stir welding, by Nguyen et al. [25] in thermomechanical modelling of friction effects in granular flow, and by Rojek [19] in a thermomechanical discrete element model of rock cutting. The explicit forward Euler scheme was adopted by Quintana-Ruiz [26] to compute the time evolution of the thermomechanical system, and by Paiva Teixeira et al. [27] to investigate transient temperature regime in a thermomechanical model of sintering. Explicit time integration was used by Morimoto et al. [11] and by Nisar et al. [28] to solve thermal problems.

Although electric current flow in granular materials is usually solved as a steady-state problem with no need for time integration, e.g. [12, 20], it was shown by Nisar et al. [21] that the steady-state problem of electric current flow can be solved iteratively using the forward Euler scheme.

Explicit time integration methods are simple to implement and are very fast in solving a single time step, but they have the disadvantage of conditional stability, which limits the time step below a certain critical value. This may lead to a very large number of time steps and make the whole explicit solution inefficient. In the explicit dynamics, the critical time step can be artificially increased by mass scaling. However, this affects the solution, and therefore its use has limitations [29]. There are some possibilities to increase the computational efficiency of transient heat transfer simulations by scaling parameters [30], however, this is possible for some special problems.

An alternative is to search for integration methods with better stability properties. Oñate et al. [31] derived an explicit procedure for the first-order differential equations allowing for larger time steps using the so-called Finite Increment Calculus (FIC). In this work, we will investigate the super-time-stepping (STS) acceleration scheme. The STS scheme speeds up explicit time-stepping for parabolic problems. The concept of STS is quite old. It was presented by Gentzsch [32] for time integration of parabolic equations combined with the finite difference spatial discretisation. It was used to solve the heat transient equation in the FEM by Droux [33]. Alexiades et al. [34, 35] presented the development of a variant of Gentzsch's method for parabolic equations spatially discretised with the finite difference method. Lewis et al. [36] used the STS scheme for irregular finite element meshes to solve a heat transfer problem from the casting industry. Gurski and O'Sullivan developed the STS algorithm for non-symmetric parabolic problems in [37] and studied its stability in [38]. Pelovska [39] adapted and modified STS algorithm to analyse numerically age-dependent population models with spatial diffusion. Barnaś and Bieniasz [40, 41] applied the STS technique to nonlinear diffusion equations in electrochemistry. A comparison of the STS scheme with new fast and accurate explicit time integration schemes for FE solution of the heat conduction problem has been recently reported by Oñate et al. [42].

All the authors investigating the STS method confirm its outstanding performance—significant speedup with sufficiently good accuracy. Despite this, it has not become commonly used in numerical engineering analyses. It is better known among mathematicians working in partial differential equations. The STS scheme for time integration is usually combined with the finite difference method for spatial discretisation. It is hardly known in the finite element method community [33, 36, 42], and it has not been used in the discrete element method yet.

The objective of the present paper is to present the implementation and validation of the STS scheme in the discrete element method for transient thermal and electrical problems, as well as for coupled thermoelectric problems. Numerical tests focus on the efficiency and accuracy obtained with the STS scheme. Efficiency is measured by the speedup of the STS simulation with respect to the standard explicit analysis. The standard explicit solution is also used as the reference solution to assess the accuracy of the STS simulation.

The present work is limited to thermal/electric transient transport simulations on fixed granular networks, in

the absence of any dynamics. In many practical applications involving granular media, transport processes such as heat conduction and electrical conduction occur in static or quasi-static particle assemblies, where particle motion is negligible or not of importance. For example, packed bed systems used in thermal energy storage [43–46] are frequently modelled using DEM approach to analyse heat transfer at particle level in the absence of any significant mechanical movement/dynamics. Haddad et al. [47] performed DEM analysis of heat conduction in composite materials using the DEM as a discretisation method of a continuous medium. The configuration of granular systems can be generated using geometric constructive methods, e.g. [43, 46, 47] or by prior dynamic DEM simulation, e.g. [44, 45]. DEM simulations of powder sintering produced DEM geometries, which were subsequently used for DEM thermal and electrical analyses to evaluate effective electrical and thermal conductivity in sintered porous materials [21, 28]. Various applications and models of the DEM for thermal simulations have been reviewed by Peng et al. [48]. These studies illustrate that the DEM is often used in the absence of coupled mechanical evolution to provide a solution for transient transport phenomena in static granular assemblies. The present is aimed to show a possibility to significantly accelerate the solution of such problems.

The rest of the paper is organised as follows. Section 2 will present the formulation and governing equations of the discrete element method for thermal, electric and thermoelectric problems. Section 3 presents the standard explicit forward Euler time integration scheme of the first-order differential equations describing transient thermal and electrical problems. The conditional stability of the forward Euler scheme is discussed. The stability criterion and critical time steps are specified. The idea of the super-time stepping method is introduced in Sect. 4. Modification of the stability criterion and sub-stepping, maximising the length of the superstep, are presented. The theoretical speedup of the STS for various parameters is analysed. Implementation of the STS method in the explicit solution algorithm is briefly outlined in Sect. 5. Approximate assessment of the critical time step for the standard explicit solution is presented in Sect. 6, and adaptation of the STS algorithm for coupled thermoelectric problems is commented in Sect. 7. Conductance model for thermal and electrical analysis is presented in Sect. 8. The STS performance is investigated in Sect. 9. First, the STS is applied to transient thermal analysis on a cylindrical discrete element sample in Sect. 9.1, and then, thermoelectric analysis is performed in Sect. 9.2. In both studies, the efficiency and accuracy of the STS scheme for different combinations of parameters were investigated. Finally, Sect. 10 summarises the results of the investigation on the STS performance and applicability in the discrete element method. The derivation of minimum and maximum eigenvalues for thermal and electrical problems, required for STS time integration, are presented in the Appendix.

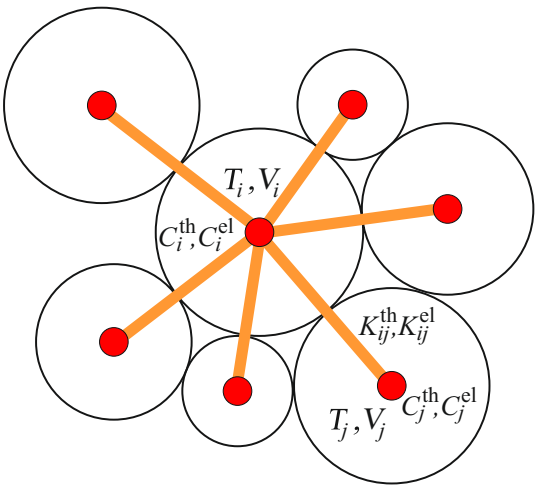

Fig. 1 Schematic of the DEM thermal and electrical models

2 Formulation of the discrete element method for thermal, electric and thermo-electric problems

2.1 Problem definition

We will consider transient problems of heat conduction and electric current in a granular material represented by an assembly of spherical particles (discrete elements). We will study these problems as independent as well as coupled ones. Electrically and thermally conductive bars are assumed to connect the particle centres as shown in Fig. 1.

It is assumed that thermal and electrical capacitances are concentrated at the particle centres, and the temperature and electric potential at the particle centres represent respective average particle quantities. We will analyse the temperature or electric potential evolution under prescribed boundary conditions. In the coupled problem, we will consider electric current flow, heat generation due to the Joule effect, heat absorption and conduction.

2.2 Equations for thermal problem

The thermal problem is governed by the first law of thermodynamics, which implies the heat balance law. The rate of thermal energy stored in each particle should be in balance with the rate of heat flow through the heat transfer branches and any other heat source [49]. This can be written for the i-th particle in the following form:

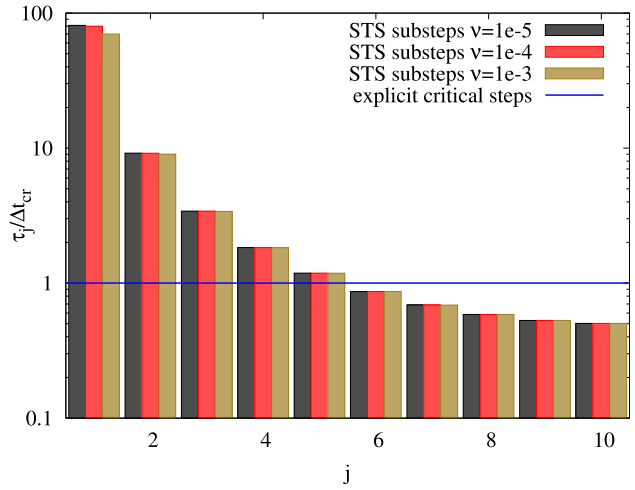

Fig. 2 STS substeps within the superstep for $N_\tau = 10$ compared to the explicit critical step

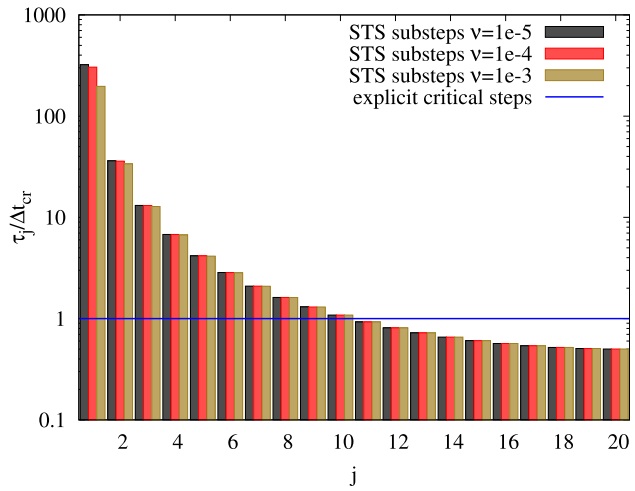

Fig. 3 STS substeps within the superstep for $N_\tau = 20$ compared to the explicit critical step

$$C_i^{\mathrm{th}}\dot{T}_i + \sum_{j=1}^{n_i^c} K_{ij}^{\mathrm{th}}(T_i - T_j) = Q_i\,, \tag{1}$$

where T_i and T_j are particle temperatures, and K_{ij}^{th} is the conductance of the bar connecting the particles *i* and *j*, and n_i^c is the number of particles in contact with the *i*-th particle. C_i^{th} is the heat capacity of the *i*-th particle evaluated as

$$C_i^{\mathrm{th}} = m_i c_i^{\mathrm{th}}\,, \tag{2}$$

where m_i—particle mass, and c_i^{th}—specific heat. Q_i is the resultant heat flux for a given particle, and it may include an externally supplied heat source Q_i^{ext}, and convective and radiative heat transfer, Q_i^{conv} and Q_i^{rad}

$$Q_i = Q_i^{\mathrm{ext}} + Q_i^{\mathrm{conv}} + Q_i^{\mathrm{rad}} \tag{3}$$

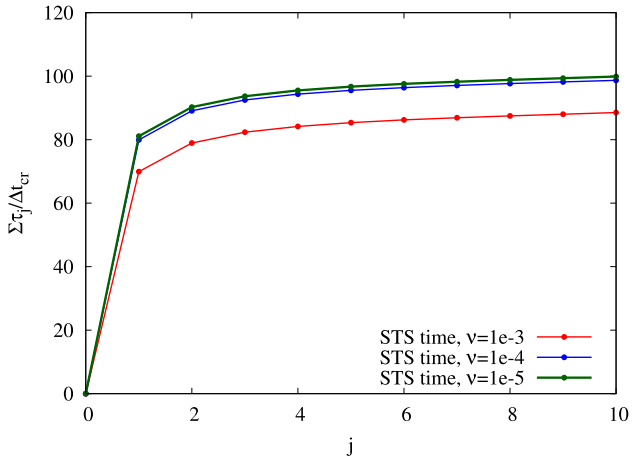

Fig. 4 Cumulative time within a superstep for $N_\tau = 10$

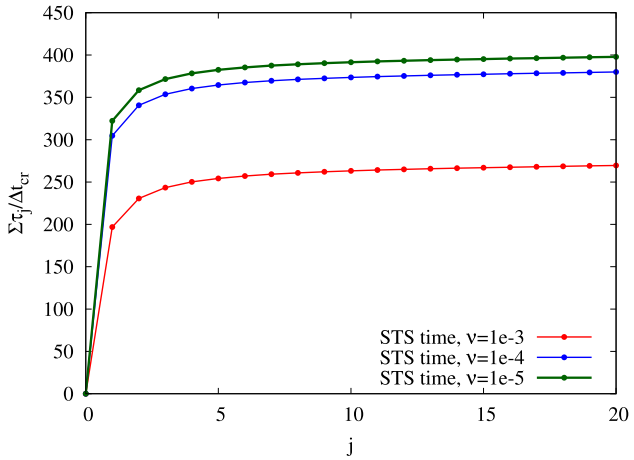

Fig. 5 Cumulative time within a superstep for $N_\tau = 20$

The term Q_i^{rad} includes radiative heat exchange between particles and the environment (for example, walls or boundaries). The interparticle radiative heat transfer is not included in the implemented algorithm.

Equation (1) can be written in a global matrix form (for all the nodes):

$$\mathbf{C}_{\mathrm{th}}\dot{\mathbf{T}} + \mathbf{K}_{\mathrm{th}}\mathbf{T} = \mathbf{Q} \tag{4}$$

where vector $\mathbf{T}$ contains the unknown nodal temperatures $\mathbf{T} = \{T_1, T_2, \ldots, T_{N_p}\}^{\mathrm{T}}$, N_p is the number of particles with unknown temperatures, vector $\mathbf{Q}$ contains nodal heat fluxes $\mathbf{Q} = \{Q_1, Q_2, \ldots, Q_{N_p}\}^{\mathrm{T}}$. The global thermal capacitance matrix $\mathbf{C}_{\mathrm{th}}$ is diagonal, $\mathbf{C}_{\mathrm{th}} = \mathrm{diag}(C_1^{\mathrm{th}}, C_2^{\mathrm{th}}, \ldots, C_{N_p}^{\mathrm{th}})$. The global thermal conductance matrix $\mathbf{K}_{\mathrm{th}}$ is assembled from the conductances of all the connections K_{ij}^{th}. The conductance matrix $\mathbf{K}_{\mathrm{th}}$ is analogous to the stiffness matrix in the FEM, and it is symmetric and positive-definite.

2.3 Equations for electric problem

In view of the analogy between electrical and thermal conduction, cf. [50], the equation for the electric problem can be written analogously to Eq. (1) as follows

$$C_i^{\mathrm{el}}\dot{V}_i + \sum_{j=1}^{n_i^c} K_{ij}^{\mathrm{el}}(V_i - V_j) = I_i\,, \tag{5}$$

where voltage V corresponds to temperature T, current I to heat flux Q, electric capacitance C^{el} to thermal capacitance C^{th}, and electric conductance K^{el} to thermal conductance K^{th}. Unlike particle heat flux given by Eq. (3), electric current I_i does not include any convection- or radiation-related contribution. Although, in general, there can be a convection electric current or an electric charge flow generated by exposure to a form of radiation, in the present work, we have not considered any such phenomena. Equation (5) expresses the law of conservation of electric charge for the electric circuit nodes connected to the ground via a capacitor. In the models of electric current flow in granular materials, electric capacity can be treated as an algorithmic parameter, cf. [21].

The set of Eq. (5) for the whole system of N_p particles with unknown potentials can be written in the matrix form analogous to Eq. (4) as follows:

$$\mathbf{C}_{\mathrm{el}}\dot{\mathbf{V}} + \mathbf{K}_{\mathrm{el}}\mathbf{V} = \mathbf{I} \tag{6}$$

where the following global vectors and matrices are introduced: $\mathbf{V} = \{V_1, V_2, \ldots, V_{N_p}\}^{\mathrm{T}}$, $\mathbf{I} = \{I_1, I_2, \ldots, I_{N_p}\}^{\mathrm{T}}$, $\mathbf{C}_{\mathrm{el}} = \mathrm{diag}(C_1^{\mathrm{el}}, C_2^{\mathrm{el}}, \ldots, C_{N_p}^{\mathrm{el}})$, $\mathbf{K}_{\mathrm{el}}$ is assembled from the conductances of all the branches in the network K_{ij}^{el}.

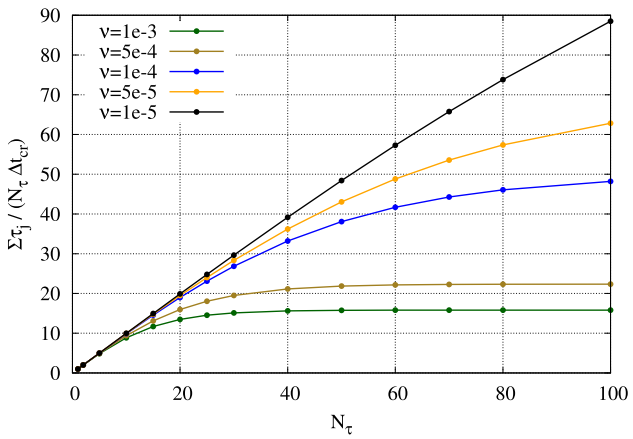

Fig. 6 Theoretical speedup achieved with various N_τ and ν values

2.4 Coupled thermoelectric problem

We will consider a coupled thermoelectric problem with Joule heating as a coupling term. Heat generated due to the Joule effect will be evaluated in the solution of the electric problem and passed to the solution of the thermal problem. The rate of Joule heat generation Q_{ij}^{Joule} in the branch connecting particles *i* and *j* is given by

$$Q_{ij}^{\mathrm{Joule}} = K_{ij}^{\mathrm{el}}(V_j - V_i)^2 = I_{ij}^2 R_{ij}^{\mathrm{el}}\,, \tag{7}$$

where K_{ij}^{el} and R_{ij}^{el} is the electrical conductance and resistance of the particle connection, respectively, $(V_j - V_i)$ is the potential difference between *j*-th and *i*-th particle, and I_{ij} is the current between the two particles. Joule heating generated in the particle connection is distributed to the particles proportionally to their contributions to the resultant resistance and included into the resultant heat flux given by Eq. (3).

3 Explicit time integration

Both problems, thermal and electric ones, are described by the systems of the first-order ordinary differential equations (ODE), (4) and (6), respectively. Let us present Eqs. (4) and (6) in a general form as follows:

$$\mathbf{C}\dot{\mathbf{X}} + \mathbf{K}\mathbf{X} = \mathbf{Y} \tag{8}$$

where $[\mathbf{C}, \mathbf{K}, \mathbf{X}, \mathbf{Y}]$ is either $[\mathbf{C}_{\mathrm{el}}, \mathbf{K}_{\mathrm{el}}, \mathbf{V}, \mathbf{I}]$ or $[\mathbf{C}_{\mathrm{th}}, \mathbf{K}_{\mathrm{th}}, \mathbf{T}, \mathbf{Q}]$. $\mathbf{X}$ is unknown function of time *t*, whereas $\mathbf{Y}$ is a given function of time, and $\mathbf{C}$ and $\mathbf{K}$ are positive definite constant matrices. Additionally, the matrix $\mathbf{C}$ is diagonal, and we can easily transform Eq. (8) into the following form

$$\dot{\mathbf{X}} + \mathbf{A}\mathbf{X} = \mathbf{B} \tag{9}$$

where

$$\mathbf{A} = \mathbf{C}^{-1}\mathbf{K}, \tag{10}$$

$$\mathbf{B} = \mathbf{C}^{-1}\mathbf{Y}. \tag{11}$$

Given an initial value of $\mathbf{X}$

$$\mathbf{X}(0) = \mathbf{X}^0\,, \tag{12}$$

the solution of the system (9) is obtained employing a suitable time integration scheme. To integrate the system of the first-order ODEs given by Eq. (9), we use the forward Euler

explicit scheme, in which the solution for time t^{n+1} can be obtained from the known state at time t^n as follows:

$$\mathbf{X}^{n+1} = (\mathcal{I} - \Delta t\mathbf{A})\mathbf{X}^n + \mathbf{B}^n\Delta t\,, \tag{13}$$

where $\Delta t = t^{n+1} - t^n$, and $\mathcal{I}$ is the identity matrix.

The solution of the system of Eq. (8) given by Eqs. (9)–(13) employs the inverse of the capacitance matrix $\mathbf{C}$, which for the diagonal matrix is trivially obtained by taking the inverses of the diagonal elements. Therefore, the explicit solution is computationally efficient. However, the disadvantage of the explicit scheme (13) is its conditional stability. The stability of the numerical integration prevents oscillation or amplification of the solution errors.

Let us suppose that the initial condition $\mathbf{X}^0$ is perturbed with ε^0. The perturbed solution $\tilde{\mathbf{X}}$ satisfies the initial value problem:

$$\dot{\tilde{\mathbf{X}}} + \mathbf{A}\tilde{\mathbf{X}} = \mathbf{B} \quad \text{with} \quad \tilde{\mathbf{X}}(0) = \mathbf{X}^0 + \varepsilon^0\,. \tag{14}$$

Let us denote the difference between the perturbed and exact solutions as $\varepsilon(t)$

$$\varepsilon(t) = \tilde{\mathbf{X}}(t) - \mathbf{X}(t)\,. \tag{15}$$

It can be easily seen that $\varepsilon(t)$ satisfies the following IVP:

$$\dot{\varepsilon} + \mathbf{A}\varepsilon = \mathbf{0} \quad \text{with} \quad \varepsilon(0) = \varepsilon^0\,. \tag{16}$$

The difference ε^n between the numerical solutions, $\tilde{\mathbf{X}}^n$ and $\mathbf{X}^n$, can be obtained as the solution of the IVP given by Eq. (16). The forward Euler scheme gives the relationship analogous to Eq. (13)

$$\varepsilon^{n+1} = (\mathcal{I} - \Delta t\mathbf{A})\varepsilon^n\,. \tag{17}$$

Applying the recurrence formula (17) to subsequent terms on the right-hand side of Eq. (17), we can obtain

$$\varepsilon^{n+1} = (\mathcal{I} - \Delta t\mathbf{A})^{n+1}\varepsilon^0\,. \tag{18}$$

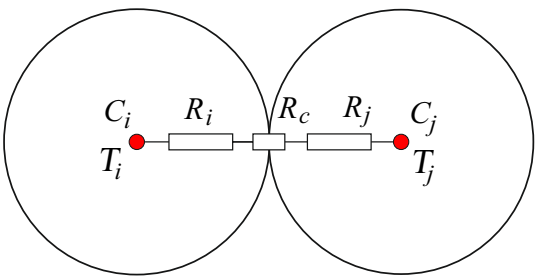

Fig. 7 Thermal pipe connecting two particles with a contact interface

The numerical solution scheme is stable if $\|\varepsilon^n\|$ is bounded for all n. This is ensured if the spectral radius of the amplification matrix is less than or equal to one for all n

$$\rho(\mathcal{I} - \Delta t\mathbf{A}) \le 1\,. \tag{19}$$

The condition (19) involves the time step Δt. The stability requires the use of small time steps, which are limited by the critical step Δt_{cr}:

$$\Delta t \le \Delta t_{\mathrm{cr}}\,. \tag{20}$$

The critical time step is determined from the condition (19) and it is given by

$$\Delta t_{\mathrm{cr}} = \frac{2}{\lambda_{\max}}\,. \tag{21}$$

where $\lambda_{\max}$ is the maximum eigenvalue of the matrix $\mathbf{A}$. It should be remarked that the matrix $\mathbf{A}$ is obtained by scaling the diagonal elements of the positive definite matrix $\mathbf{K}$ by positive inverse elements of the diagonal matrix $\mathbf{C}$, therefore, it keeps the positive definite property and all its eigenvalues are positive.

4 Super-time-stepping acceleration of the explicit scheme

The super-time stepping (STS) algorithm, as presented by Alexiades et al. [35], is based on relaxing the stability condition (19) at every time step, and instead requiring stability at the end of the cycle of N_τ steps. We will define N_τ steps denoted $\tau_1, \ldots, \tau_{N_\tau}$ making up the so-called super-step Δt_{STS}:

$$\Delta t_{\mathrm{STS}} = \sum_{j=1}^{N_\tau} \tau_j\,. \tag{22}$$

The stability condition for the super-step can be written as follows:

$$\rho\left(\prod_{j=1}^{N_\tau}(\mathcal{I} - \tau_j\mathbf{A})\right) \le 1\,. \tag{23}$$

The intermediate steps $\tau_j, j = 1, \ldots, N_\tau$, are determined by solving the problem of maximisation of the length of the superstep Δt_{STS} with the stability criterion (23) as the constraint. The solution yields the time steps τ_j in the following form [35]:

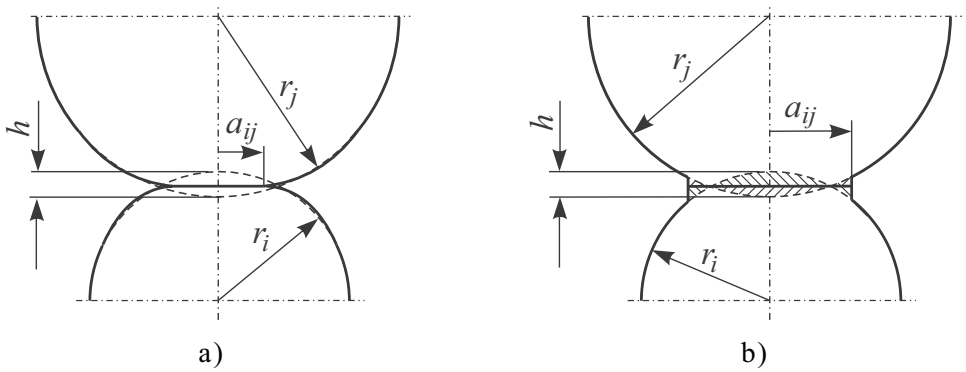

Fig. 8 Geometry of two interacting particles: **a** by contact, **b** bonded by a sintering neck

$$\tau_j = \Delta t_{\mathrm{cr}} \left[(-1+\nu) \cos\left(\frac{2j-1}{N_\tau} \frac{\pi}{2} \right) + 1 + \nu \right]^{-1}, \quad j = 1, \ldots, N_\tau, \tag{24}$$

where Δt_{cr} is determined according to Eq. (21), and ν is a certain small parameter:

$$0 < \nu < \frac{\lambda_{\min}}{\lambda_{\max}}, \tag{25}$$

with $\lambda_{\min}$ and $\lambda_{\max}$, being the minimum and maximum eigenvalues of $\mathbf{A}$. Each of the N_τ substeps has a different length as given by Eq. (24). Variation of the lengths of substeps τ_j for different values of the parameter ν for $N_\tau = 10$ and 20 is shown in the form of histograms in Figs. 2 and 3, respectively. It can be seen that the lengths of steps are decreasing with the increase of j. The substep lengths τ_j are normalised with respect to the critical time step Δt_{cr}. The first steps for $j = 1, \ldots, N_\tau/2$ are larger and the rest are smaller than Δt_{cr}. It can be seen that, particularly, the step τ_1 is much larger than Δt_{cr} as well as the other substeps τ_j for $j > 1$. Figures 2 and 3 also show the influence of the parameter ν on the length of the STS substeps. The smaller ν is, the larger STS substeps are.

The effect of the parameter ν can be observed better in Figs. 4 and 5, which show the cumulative time within a superstep for $N_\tau = 10$ and 20, respectively. It can be seen that for the smaller values of ν the time covered by a superstep is nearly $(N_\tau)^2$ larger than the critical time step:

$$\Delta t_{\mathrm{STS}} \to (N_\tau)^2 \Delta t_{\mathrm{cr}} \quad \text{if} \quad \nu \to 0\,. \tag{26}$$

In the standard explicit time integration, N_τ steps cover a time of $N_\tau \Delta t_{\mathrm{cr}}$. This means that the time covered by N_τ intermediate steps in the STS algorithm can be up to N_τ times larger than the time covered by the same number of steps in the standard explicit scheme. This, in turn, reduces the number of necessary time steps required in the analysis. The theoretical gain (speedup) of the simulation measured by the ratio $\Delta t_{\mathrm{STS}}/(N_\tau \Delta t_{\mathrm{cr}})$ for various values of N_τ and ν is plotted in Fig. 6. It can be seen that for larger values of ν the theoretical gain saturates with increasing N_τ. The theoretical maximum speedup for larger numbers of substeps N_τ is obtained for very small parameters ν. However, by decreasing the value of ν close to zero, we are approaching the stability limit of the *STS* scheme ($\nu = 0$), which is warned by Alexiades et al. [35]. We should also remember that the accuracy of the STS scheme is of order one with respect to Δt_{STS} [35]. The effect of STS parameters on efficiency and accuracy will be studied further in numerical examples.

It should be remarked that practical calculations show that the inequality (25) does not need to be strictly satisfied [35, 40]. Barnaś and Bieniasz [40] have found out that the value of ν can be chosen rather freely, without taking into account the spectral properties of the matrix $\mathbf{A}$, given by Eq. (10). It was also observed in the studies of Alexiades et al. [35], Gonzalez-Morales et al. [51], and French [52], that robust solution is achieved if ν is chosen within the interval of $0 < \nu < 1$.

5 Implementation of the STS algorithm

Implementation of the STS algorithm is straightforward [35], with few changes to the standard explicit scheme defined by Eq. (13). First, the critical time step Δt_{cr} for the forward Euler scheme is determined. Then, instead of performing time stepping with $\Delta t < \Delta t_{\mathrm{cr}}$, we execute supersteps of length Δt_{STS} composed of N_τ substeps τ_j evaluated according to Eq. (24). The substepping is performed replacing Δt in Eq. (13) with τ_j. The only additional cost is computation of the substep τ_j given by Eq. (24). We should remember that the solution is meaningful at the end of each superstep only. The STS scheme with $N_\tau = 1$ and $\nu = 0$ is reduced to the standard explicit scheme. Therefore, implementation of the STS scheme allows us to perform the normal time-integration given by Eq. (13). In principle, the choice of N_τ and ν is arbitrary. However, the STS scheme's stability and accuracy aspects should be considered. Performance, stability and accuracy of the STS scheme for

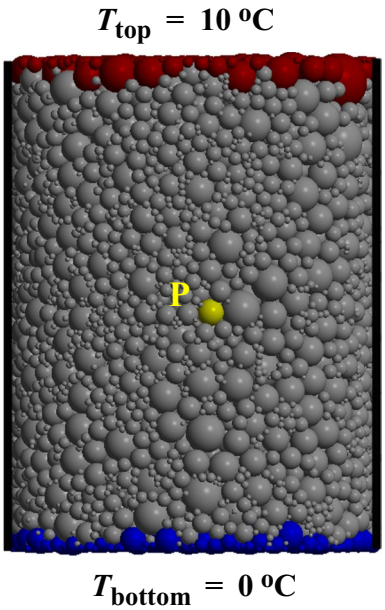

Fig. 9 Discrete element sample with definition of boundary conditions

different combinations of N_τ and ν will be studied in the numerical tests.

6 Approximate evaluation of the critical time step

In practical implementation of the explicit scheme, evaluation of the maximum eigenvalue $\lambda_{\max}$ of the matrix $\mathbf{A}$, to determine the critical time step according to Eq. (21) would be computationally costly, especially because the global matrix $\mathbf{A}$ need not be assembled. The matrix–vector multiplication $\mathbf{AX}$ is performed locally by taking contributions from two-particle connections. Accordingly, the critical time step Δt_{cr} is evaluated approximately by taking the minimum of the critical time steps $\Delta t_{ij}^{\mathrm{cr}}$ for two-particle systems and additionally scaling it by a certain safety factor α $(0 < \alpha < 1)$ [28]:

$$\Delta t_{\mathrm{cr}} \approx \alpha \min(\Delta t_{ij}^{\mathrm{cr}}) \,. \tag{27}$$

where

$$\Delta t_{ij}^{\mathrm{cr}} = \frac{C_{ij}^{\mathrm{eq}}}{K_{ij}} \,, \tag{28}$$

and K_{ij} is the conductance between particles i and j, and C_{ij}^{eq} is the harmonic mean of the capacitances C_i and C_j , cf. [28]:

$$C_{ij}^{\mathrm{eq}} = \frac{2C_iC_j}{C_i + C_j} \,. \tag{29}$$

The STS stability condition given by Eq. (23) assumes the matrix $\mathbf{A}$ to be constant during a super-step. The critical time step used in Eq. (24) is evaluated based on the maximum eigenfrequency of the matrix $\mathbf{A}$. However, in practice, Eq. (24) is implemented with the critical time step assessed with a certain safety margin α $(0 < \alpha < 1)$, cf. Equation (27). Therefore, some small changes to the matrix $\mathbf{A}$ during the super-step can be allowed without affecting the stability. Additionally, the critical time step and STS substeps can be re-evaluated after each superstep or, in the case of moderate variation of the matrix $\mathbf{A}$, every certain number of supersteps. Thus, we can expect that the STS can also be used in problems in which matrices $\mathbf{K}$ and $\mathbf{A}$ are subject to changes. The STS was used by other authors for nonlinear problems with satisfactory results. Alexiades et al. [35] observed that STS performance was very good not only in the linear case, but also for non-linear problems, although, in the latter case, no theoretical foundations were available.

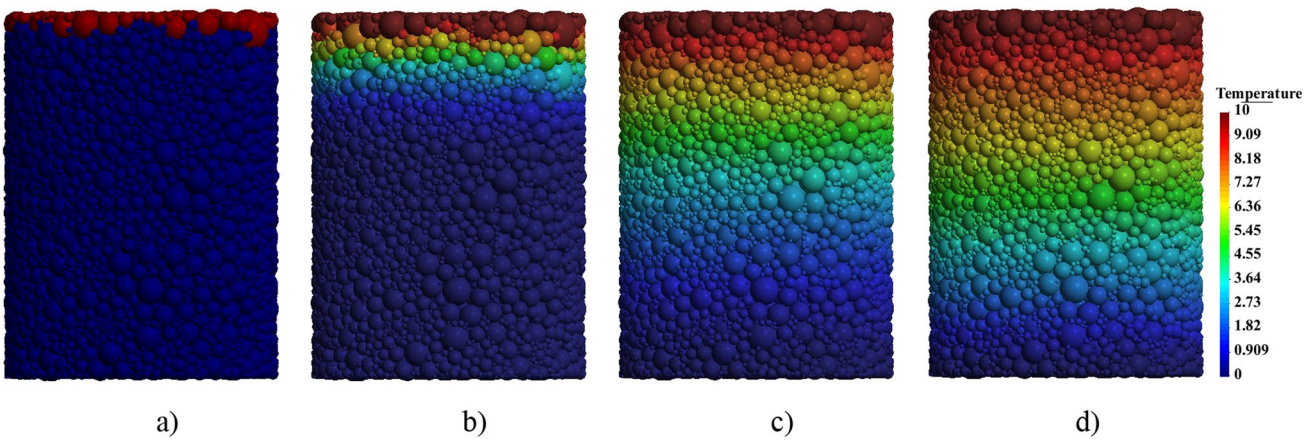

Fig. 10 Temperature (in °C) distribution in the sample at different time steps: **a** $t = 0$ ms, **b** $t = 0.02$ ms, **c** $t = 0.2$ ms, **d** $t = 1$ ms

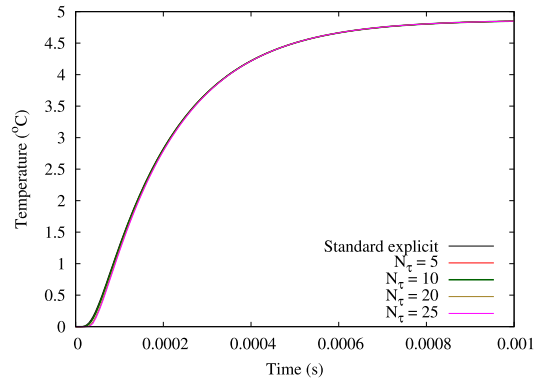

a)

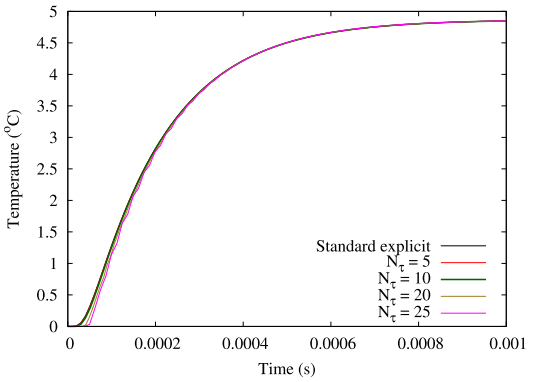

b)

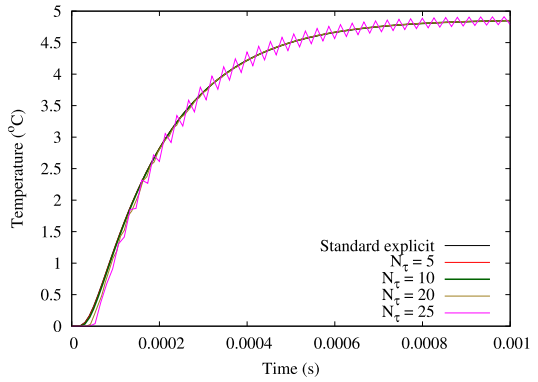

c)

Fig. 11 Comparison of temperature evolution (at particle P, Fig. 9): **a** $\nu = 1\text{e}{-3}$, **b** $\nu = 1\text{e}{-4}$, **c** $\nu = 1\text{e}{-5}$

7 STS method for the coupled thermo-electric problem

Implementation of the coupled thermo-electric discrete element model using the standard explicit time integration was presented in [53]. The thermo-electric problem is defined by the set of equations for heat conduction (4) coupled by the Joule heating term given by Eq. (7) with the set of equations for the electric problem (6). Here, we consider one-way coupling. However, it can be easily extended to two-way coupling by taking into account the temperature-dependence of the electric properties. The sets of equations (4) and (6), complemented by adequate initial conditions, are integrated in time in a staggered manner. The STS scheme is employed in the time integration of thermal and electric problems, taking the STS superstep's unified lengths. The STS substeps are evaluated according to Eq. (24) using the critical time step Δt_{cr} as minimum of the critical time steps calculated for both problems:

$$\Delta t_{\text{cr}} = \min(\Delta t_{\text{cr}}^{\text{el}}, \Delta t_{\text{cr}}^{\text{th}})\,. \tag{30}$$

8 Conductance model

The effective conductance K_{ij} of the branch connecting particles *i* and *j* can be obtained assuming the connection in a series of elements representing contributions of particles, K_i and K_j, and the inter-particle interface, K_c, as shown in Fig. 7. The effective conductance can be obtained from the following relationship

$$\frac{1}{K_{ij}} = \frac{1}{K_i} + \frac{1}{K_j} + \frac{1}{K_c}\,, \tag{31}$$

which can be rewritten as follows, cf. [28]::

$$K_{ij} = \frac{K_i K_j K_c}{K_i K_j + K_j K_c + K_i K_c}\,. \tag{32}$$

Taking advantage of the thermal-electrical analogy [50], the conductance model presented here can be applied to electrical as well as thermal problems.

The contributions of the particles, K_i and K_j to the effective electric or thermal conductance K_{ij} will be evaluated using the linear relationship obtained in [54]:

$$K_i = 1.08\kappa_i \pi a_{ij} \quad K_j = 1.08\kappa_j \pi a_{ij}\,, \tag{33}$$

where κ_i and κ_j are the electric or thermal bulk conductivities of particles *i* and *j*, and a_{ij} denotes the radius of the contact area or neck connecting two particles.

The radius of the contact area or the neck size for two overlapping particles defined by their positions and radii (Fig. 8) can be calculated based on suitable contact or sintering models, respectively.

If we assume the two non-bonded particles overlapping by *h* (Fig. 8a) are elastic, the contact radius can be evaluated using the Hertz contact model for two elastic spheres as, e.g. [55, 56]:

$$a_{ij} = \sqrt{0.5\, r_{\text{eff}}\, h}\,, \tag{34}$$

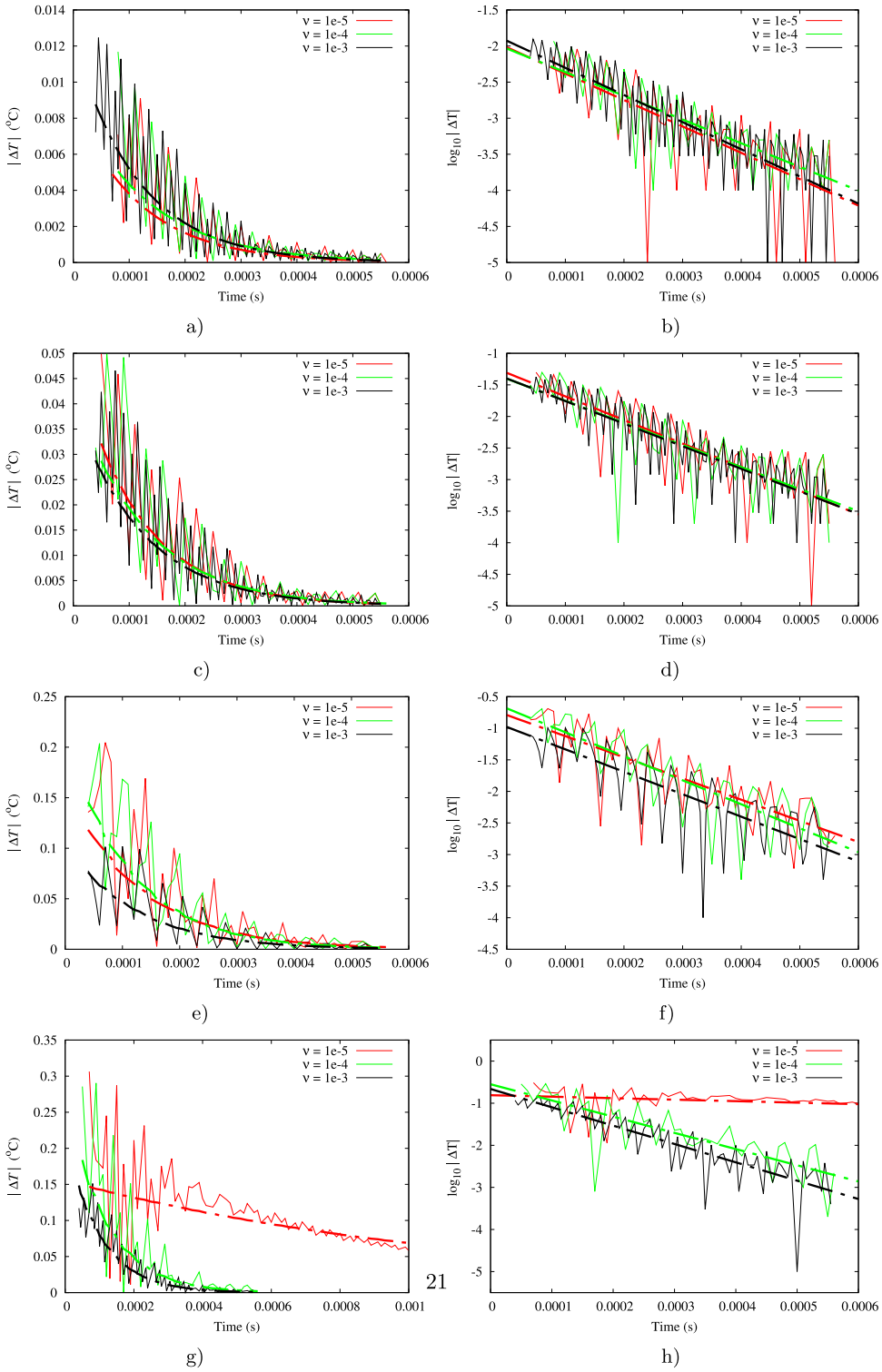

Fig. 12 Error in temperature evolution (at particle P, Fig. 9): **a**, **b** $N_\tau = 5$, **c**, **d** $N_\tau = 10$, **e**, **f** $N_\tau = 20$, **g**, **h** $N_\tau = 25$; **a**, **c**, **e**, **g**—normal scale with exponential fitted trendlines; **b**, **d**, **f**, **h**—log scale with linear fitted trendlines

where

$$r_{\text{eff}} = \frac{2 r_i r_j}{r_i + r_j}. \tag{35}$$

The relationship between contact radius a_{ij} and the overlap h for plastic particles has been obtained by Larsson et al. [57] in the following form:

$$a_{ij} = \sqrt{f_c^2 \, r_{\text{eff}} \, h}\,, \tag{36}$$

Table 1 Analysis of error in temperature evolution

ν	N_τ	ΔT_{mean} (°C)	k (s^{-1})	R^2
1e−3	5	2.3748e−3	8.6628e3	0.65
	10	8.8457e−3	8.2452e3	0.65
	20	2.2955e−2	8.2233e3	0.63
	25	3.2215e−2	1.0058e3	0.71
1e−4	5	1.9996e−3	7.5579e3	0.60
	10	9.8804e−3	8.0641e3	0.57
	20	4.1444e−2	8.7700e3	0.70
	25	5.7081e−2	8.9013e3	0.62
1e−5	5	1.7720e−3	8.4179e3	0.47
	10	9.6847e−3	8.6044e3	0.58
	20	4.1347e−2	7.7703e3	0.63
	25	1.1409e−1	8.1627e2	0.16

where f_c^2 is a function of the Hollomon strain-hardening exponent m. The function $f_c^2 = f_c^2(m)$ obtained by the FEM analyses varies from 0.5 for linear hardening ($m = 1$) to 1.45 for perfect plasticity ($m = \infty$).

The neck radius for a pair of sintered particles is evaluated considering the sintering geometry shown in Fig. 8b. The sintering neck is formed by the diffusive mass transport from the grain boundary to the neck surface. The two-particle sintering model proposed by Coble [58] assumes that the material from the particle intersection is distributed to the neck. The neck size for a pair of unequal particles predicted by Coble [59] is given by

$$a_{ij} = \sqrt{2\, r_{\text{eff}}\, h}\,. \tag{37}$$

Equation (37) overestimates the neck size, and the error increases with an increase in the overlap. The correction to the formula (37) has been introduced by Rojek et al. [54]

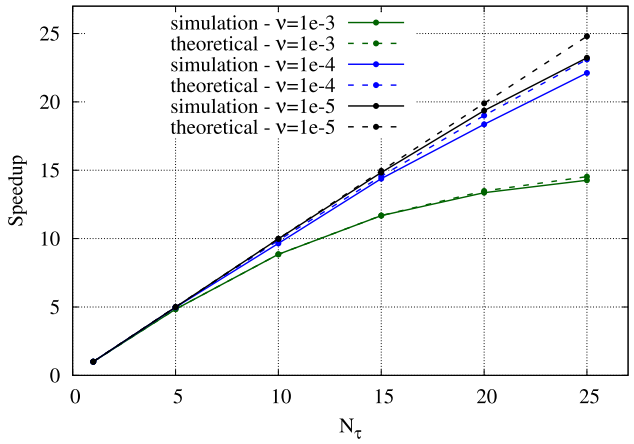

Fig. 13 Comparison of theoretical speedup and that achieved from simulations (CPU time of time stepping only)

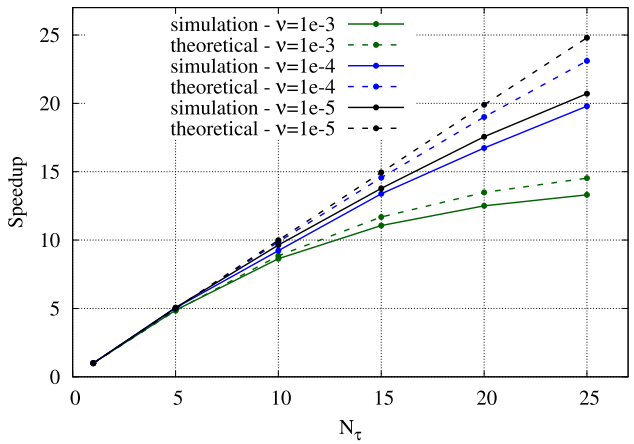

Fig. 14 Comparison of theoretical speedup and that achieved from simulations (total CPU time)

Table 2 Performance metrics for the simulations of the thermal problem

STS parameters		Total No. of STS substeps	Total CPU time (s)	CPU time (s) of time stepping	Speedup (total CPU time)	Speedup (time stepping)
ν	N_τ					
0	1	46561	1283	1269.9	1.00	1.00
1e−3	5	9610	263	255.7	4.87	4.97
	10	5260	149	141.1	8.63	9.00
	15	3990	116	108.7	11.06	11.68
	20	3460	103	95.1	12.51	13.36
	25	3225	96	89.0	13.31	14.27
1e−4	5	9335	254	246.8	5.04	5.15
	10	4720	139	131.6	9.22	9.65
	15	3195	96	88.3	13.39	14.38
	20	2460	77	69.2	16.73	18.36
	25	2025	65	57.4	19.79	22.12
1e−5	5	9310	254	246.1	5.06	5.12
	10	4660	133	125.8	9.63	9.92
	15	3120	93	85.6	13.78	14.82
	20	2340	73	65.6	17.56	18.82
	25	1900	62	54.7	20.70	23.14

by imposing the criterion of volume preservation. The corrected model presented in [54] is used in the present work in the numerical simulations.

The contact/neck radius a_{ij} affects the particle conductance given by Eq. (33) as well as the interface conductance K_c. The interface conductance is given as follows, cf. [21, 28]:

$$K_c = \epsilon_{ij}\kappa_{ij}^{\mathrm{eq}}\frac{\pi a_{ij}^2}{\delta_{\mathrm{gb}}}, \tag{38}$$

where $\kappa_{ij}^{\mathrm{eq}}$ is the equivalent transverse conductivity of the bi-layered interface of thickness δ_{gb}:

$$\kappa_{ij}^{\mathrm{eq}} = \frac{2\kappa_i\kappa_j}{\kappa_i + \kappa_j}, \tag{39}$$

and ϵ_{ij} $(0 < \epsilon_{ij} < 1)$ is the conductivity reduction factor used to reduce conductivity by a certain fraction in the grain boundary. This accounts for any porosity, impurity or roughness in the grain boundary region.

The two parameters defining conductance of the grain boundary, ϵ_{ij} and δ_{gb}, are treated as fitting parameters in the calibration of the discrete element model. The present work takes advantage of the calibration performed in our earlier works on evaluation of effective thermal [28] and electrical [21] conductivities of sintered geometries using DEM. In the case of different particle materials, these parameters should be determined for each pair of materials. Herein, all the particles are from the same material, with thermal or electrical conductivity κ. Thus, we have

$$\kappa_i = \kappa_j = \kappa_{ij}^{\mathrm{eq}} = \kappa, \tag{40}$$

$$\epsilon_{ij} = \epsilon. \tag{41}$$

9 Numerical examples

9.1 Thermal analysis using the STS scheme

Transient thermal analysis was carried out using a cylindrical discrete element sample of diameter 123.6 μm and height 166 μm shown in Fig. 9.

The sample is composed of 17515 bonded particles with diameters of 1.5 μm to 20 μm representing partially sintered intermetallic NiAl powder. This is one of the samples (with a relative density of 0.784) studied in [28], where effective conductivity was evaluated using DEM thermal model, and the grain-boundary parameters (δ_{gb} and ϵ) were calibrated and validated with experimental measurements. Herein, heat conduction analysis was performed with the following model parameters:

- density $\rho = 5910\ \mathrm{kg\,m^{-3}}$,
- specific heat capacity $c^{\mathrm{th}} = 640$ J/(kg K),
- thermal conductivity $\kappa^{\mathrm{th}} = 85\ \mathrm{W/(m\,K)}$,
- thickness of the grain boundary $\delta_{\mathrm{gb}} = 0.2\mu m$,
- conductivity-reduction factor for the grain boundary $\epsilon = 0.17$,
- safety factor for assessment of the critical time step $\alpha = 0.3$.

Thermal insulation of the sample in the radial direction was assumed. The initial temperature of 0°C was prescribed to the whole sample. Heat conduction in the sample was induced by setting and holding constant the temperatures of 10°C and 0°C to the top and bottom layers of the particles, as shown in Fig. 9. The transient heat flow during 1 ms was simulated. First, the analysis was started from the simulation with the standard explicit forward Euler method. Figure 10 shows the evolution of temperature distribution in the

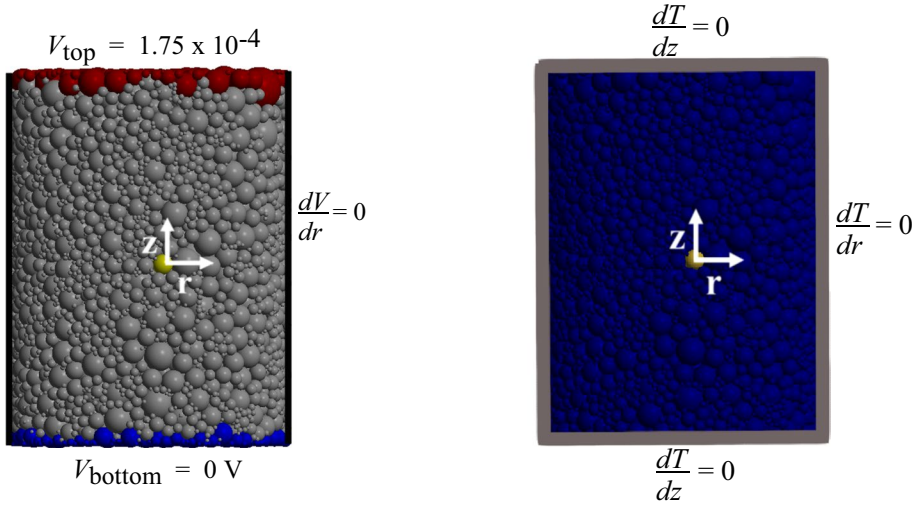

Fig. 15 DEM problem definition: **a** electrical boundary conditions, **b** thermal boundary conditions

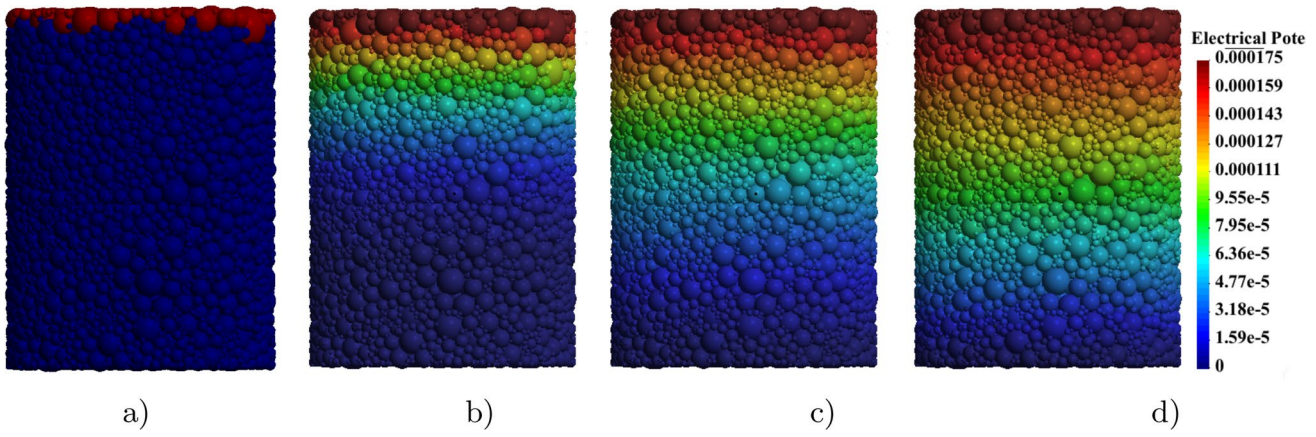

Fig. 16 Distribution of the electric potential (in V) at different time steps of the transient phase: **a** $t = 0$ ms, **b** $t = 2\text{e}{-5}$ s, **c** $t = 6\text{e}{-5}$ s, **d** $t = 4\text{e}{-4}$ s

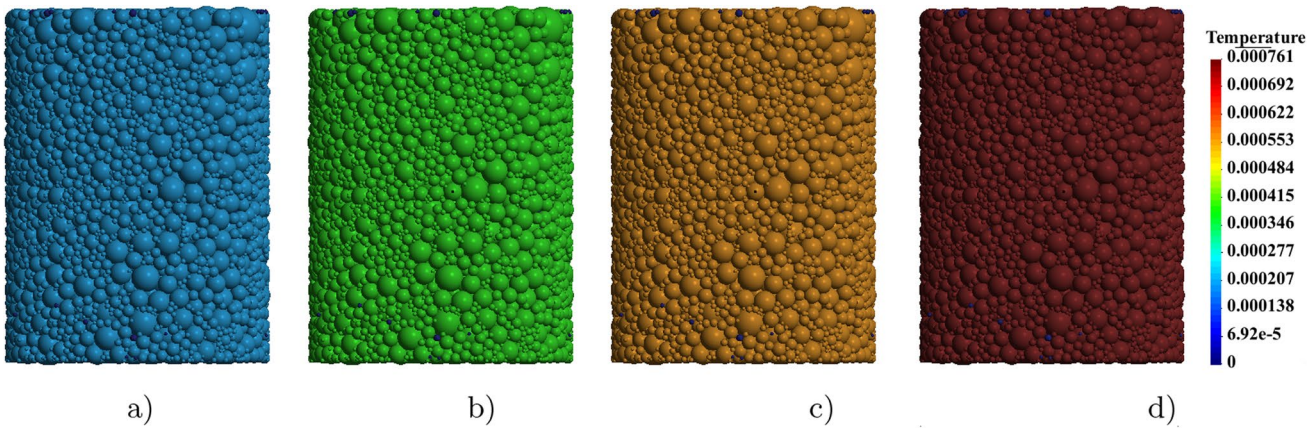

Fig. 17 Temperature (in °C) distribution in the sample at different time steps: **a** $t = 1\text{e}{-3}$, **b** $t = 2\text{e}{-3}$ s, **c** $t = 3\text{e}{-3}$ s, **d** $t = 4\text{e}{-3}$ s

sample obtained using the standard explicit time integration. Initially, we can observe a large temperature gradient at the upper part of the sample and a very small one at the lower part. Gradually, the temperature distribution varies to reach a linear profile along the axis at the end of the simulation, indicating the steady-state heat flow.

The STS simulations were performed for different combinations of STS parameters $N_\tau \in \{5, 10, 20, 25\}$ and $\nu \in \{1\text{e}{-5},\ 1\text{e}{-4},\ 1\text{e}{-3}\}$. The ratio of the minimum and maximum eigenvalues, estimated for this problem in Appendix A.1, is $\lambda^{\text{th}}_{\min}/\lambda^{\text{th}}_{\max} = 1.275\text{e}{-4}$. Two of the tested values of ν, $1\text{e}{-5}$ and $1\text{e}{-4}$, are in the prescribed range. The third value is higher than the upper limit.

Efficiency and accuracy of the STS scheme for different values of N_τ and ν were compared to those of the standard explicit forward Euler method which was used as the reference solution. Figure 11 compares the temperature evolution at particle P at the half of the sample height (Fig. 9) for different combinations of STS parameters and the standard explicit solution (labelled with $N_\tau = 1$). All the solutions present an increase in temperature in the initial phase and stabilisation at the end, which corresponds to a quasi-state heat flow. The curves in Fig. 11a obtained with various values of N_τ and $\nu = 1\text{e}{-3}$ coincide nearly perfectly. Some divergence, especially in the transient stage, can be observed in Fig. 11b and c. The curves for the highest values of N_τ in Fig. 11b and c demonstrate oscillations which are especially pronounced in Fig. 11c (for the lowest value of ν).

Since the standard explicit solution $T_{\text{st}-\text{expl}}$ can be regarded as close to the exact solution, the difference between the STS solutions T_{STS} and $T_{\text{st}-\text{expl}}$

$$\Delta T(t) = T_{\text{STS}}(t) - T_{\text{st}-\text{expl}}(t) \tag{42}$$

can be considered an error in the STS solutions. It can be observed in Fig. 11 that the solution converges to the standard explicit solution, which means that the error decreases. The absolute errors $|\Delta T(t)|$ in the transient phase are plotted in Fig. 12a, c, e, and g, which show their rapid decrease in time. Assuming that the error decreases exponentially, the errors can be fitted by a function:

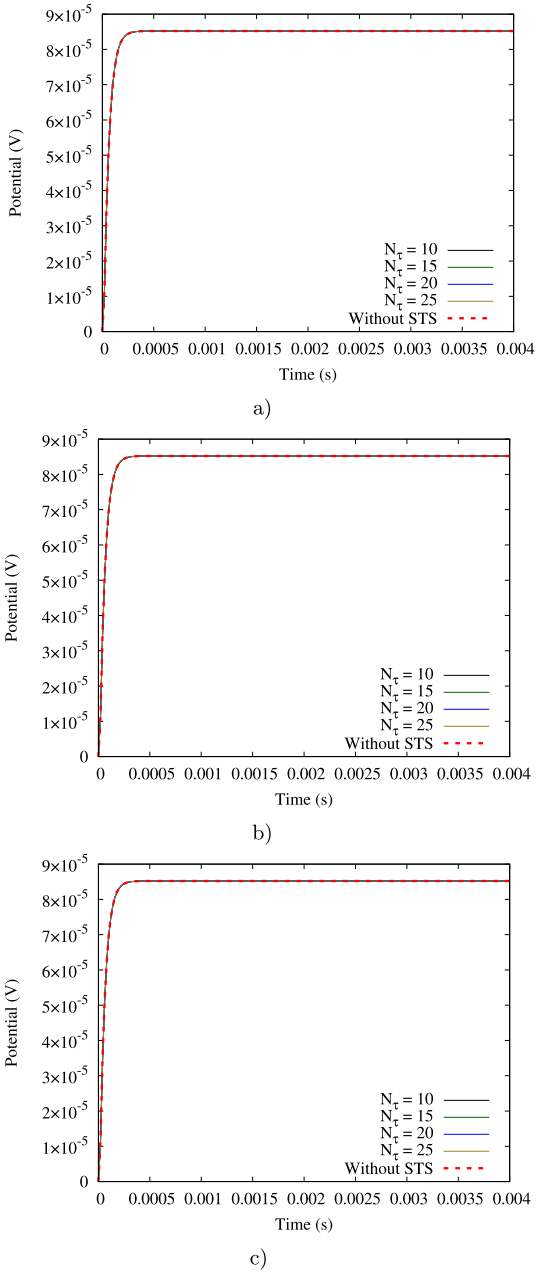

Fig. 18 Comparison of potential evolution (at particle P, Fig. 9): **a** $\nu = 1e{-}3$, **b** $\nu = 1e{-}4$, **c** $\nu = 1e{-}5$

$$|\Delta T(t)| = Z\, e^{-kt}\,, \tag{43}$$

where Z is a constant, and k is the error decay rate. To verify the assumption, the exponential relation (43) is transformed to a linear form by taking the logarithm of both sides:

$$\log_{10} |\Delta T(t)| = \log_{10} Z - \frac{k}{\ln 10}\, t\,, \tag{44}$$

where we took advantage of the relation:

$$\log_{10} e = \frac{1}{\ln 10}\,. \tag{45}$$

In accordance with the transformation given by Eq. (44) we plot $\log_{10} |\Delta T(t)|$ vs. time in Fig. 12b, d, f, and h. We perform a linear regression analysis to fit the errors with linear functions. The error plots in Fig. 12b, d, f, and h indicate that linear fitting is possible, although the coefficient of determination R^2, cf. Table 1, is relatively weak due oscillatory nature of the errors. The error decay rate k can be determined from the slope s of the linear fit of $\log_{10} |E(t)|$ given as:

$$s = -\frac{k}{\ln 10}\,. \tag{46}$$

The decay rates obtained for all parameter combinations are given in Table 1. For most cases, k has similar values. The only noticeable exception is the cases with $N_\tau = 25$ and $\nu = 1e{-}5$ where the decay rate is approximately one order slower. The decay rate k characterizes how fast the error decreases in time. However, it does not provide information about the magnitude of the error. The error magnitude is better assessed based on the exponential fits shown in Fig. 12, where both the decay constant k and the intercept Z are taken into account according to the Eqs. (43) and (44). To analyse the error quantitatively, mean absolute error (ΔT_{mean}) was evaluated as:

$$\Delta T_{\text{mean}} = \frac{\sum_{i=1}^{n_e} |\Delta T(t_i)|}{n_e}\,, \tag{47}$$

where $|\Delta T(t_i)|$ is the absolute error at time t_i and n_e is the number of output instants in the interval used for the linear fitting. ΔT_{mean} values given in Table 1 show a gradual increase with the number of STS substeps N_τ. It is understandable, since the increase of N_τ leads to an increase of the superstep Δt_{STS}, and the accuracy of the STS scheme is of order one with respect to Δt_{STS}. Thus, with the increase of N_τ and in consequence of Δt_{STS}, the error increases. The increasing trend in error with the increase of N_τ can be seen for all the values of ν; though, it is more prominent for smaller ν. Particularly, for $\nu = 1e{-}5$, ΔT_{mean} increases more noticeably as N_τ increases. for small N_τ ($N_\tau = 5, 10$), the error is nearly insensitive to the changes of parameter ν. Small variations appear for $N_\tau = 20$, while for $N_\tau = 25$, dependency of the error on the parameter ν becomes more prominent. Overall, the error increases with increasing N_τ and decreasing ν. This analysis shows that high values of N_τ combined with very low values of ν may produce unacceptably large errors.

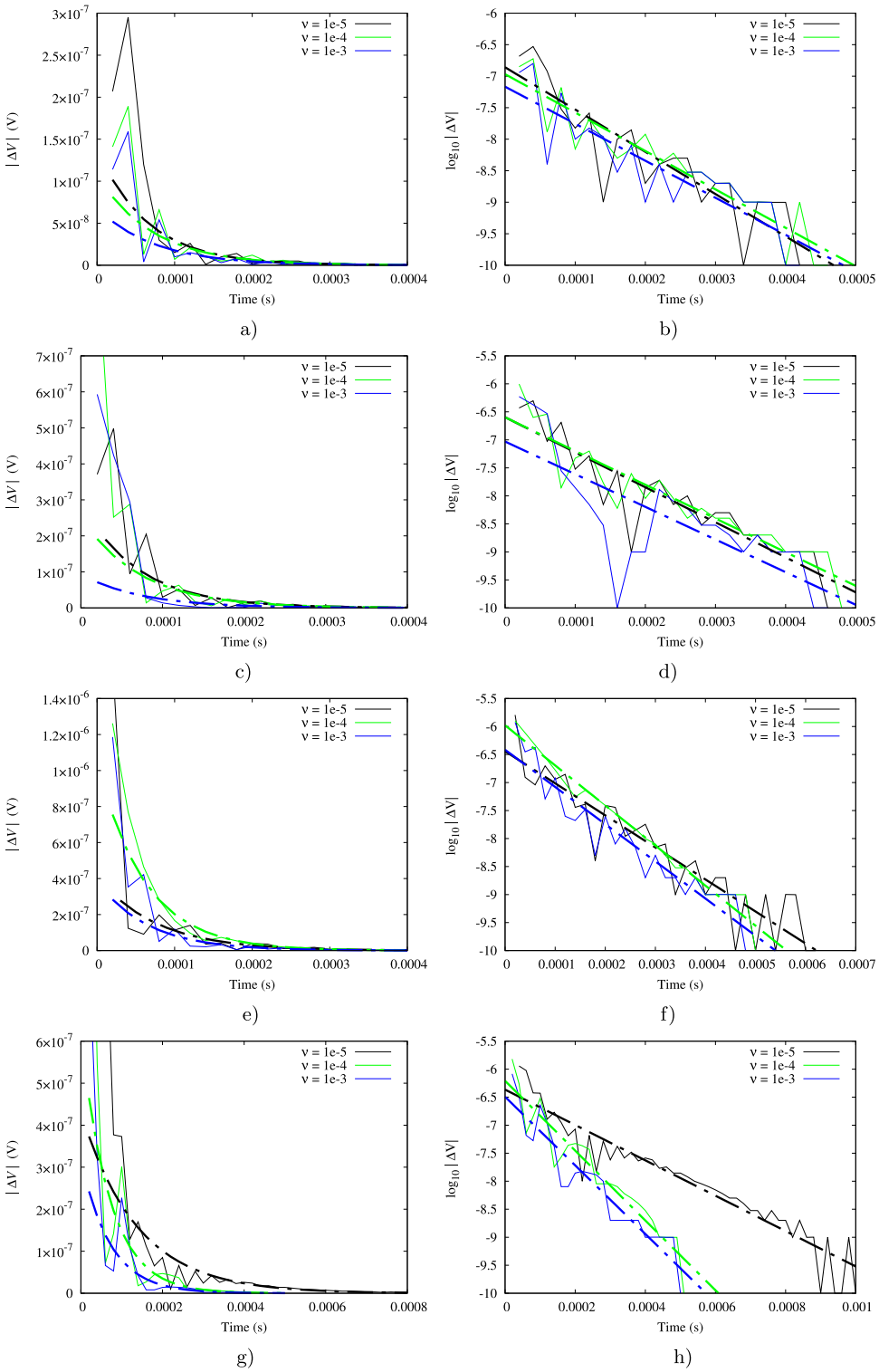

Fig. 19 Error in potential evolution (at particle P, Fig. 9): **a**, **b** $N_\tau = 10$, **c**, **d** $N_\tau = 15$, **e**, **f** $N_\tau = 20$, **g**, **h** $N_\tau = 25$; **a**, **c**, **e**, **g**—normal scale with exponential fitted trendlines; **b**, **d**, **f**, **h**—log scale with linear fitted trendlines

On the other hand side, Fig. 6 demonstrates that the larger value of N_τ and smaller value of ν are, the bigger gains in computational efficiency can be expected. Parameter combinations that yield higher accuracy are unfavourable with respect to computational efficiency. Performance metrics obtained in the simulations with various combinations of STS parameters are given in Table 2.

Data for $\nu = 0$ and $N_\tau = 1$ represent the performance of the standard explicit scheme. The performance is measured in terms of CPU time. Simulations were performed on the PC workstation equipped with an AMD Ryzen Threadripper

Table 3 Analysis of error in potential evolution

ν	N_τ	ΔV_{mean} (V)	k (s^{-1})	R^2
1e−3	10	1.8914e−8	1.3532e4	0.77
	15	6.1143e−8	1.3421e4	0.58
	20	9.5380e−8	1.5290e4	0.89
	25	6.9684e−8	1.4099e4	0.89
1e−4	10	2.1535e−8	1.4034e4	0.87
	15	7.3712e−8	1.3856e4	0.86
	20	1.3448e−7	1.6475e4	0.97
	25	1.1856e−7	1.4350e4	0.90
1e−5	10	3.5343e−8	1.5445e4	0.77
	15	5.9004e−8	1.4395e4	0.82
	20	8.0822e−8	1.3177e4	0.86
	25	1.2016e−7	7.2688e3	0.89

2950X processor with a base clock frequency of 3.5 GHz. The CPU time is given for the whole analysis and for the time-stepping (without input of the data and initial calculations). All the data were collected from the simulations with a minimum number of output operations. The speedup obtained with STS algorithm is evaluated as the ratio of the CPU times of the standard explicit and STS simulations. The speedups obtained for various combinations of STS parameters are compared with the theoretical speedups in Figs. 13 and 14. It can be observed in Fig. 13 that the speedup measured for time-stepping is very close to the theoretical speedup. The speedups obtained for the whole analyses (Fig. 14) are only slightly lower. We can observe that the speedups of up to 20 can be obtained for $N_\tau = 25$ and $\nu = 1\text{e}{-4}$ and $\nu = 1\text{e}{-5}$. However, the error analysis carried out above shows that the errors of simulations with high values of N_τ and very low values of ν can be too large. Practical speedup obtained in simulations with a smaller error is up to 15, for instance, solutions for $\nu = 1\text{e}{-3}$ and all the considered values of N_τ or for $N_\tau = 15$ and all the values of ν.

9.2 Thermo-electric analysis using the STS scheme

Thermo-electric simulations were performed on the sample used in the thermal analysis. The flow of the electric current through the sample under a prescribed voltage was analysed in the electric problem. Definition of the boundary conditions for the electric problem is shown in Fig. 15a. Electrical potential of 1.75×10^{-4} V was assigned to the top layer of particles and 0 V to the bottom layer. The insulation was assumed for the lateral surface of the sample. One-way coupling between electrical and thermal problems was considered. The Joule heat evaluated in the electrical solution was passed at each step to the thermal problem. Heat absorption and conduction were analysed in the sample. The temperature increase and its distribution in the sample were

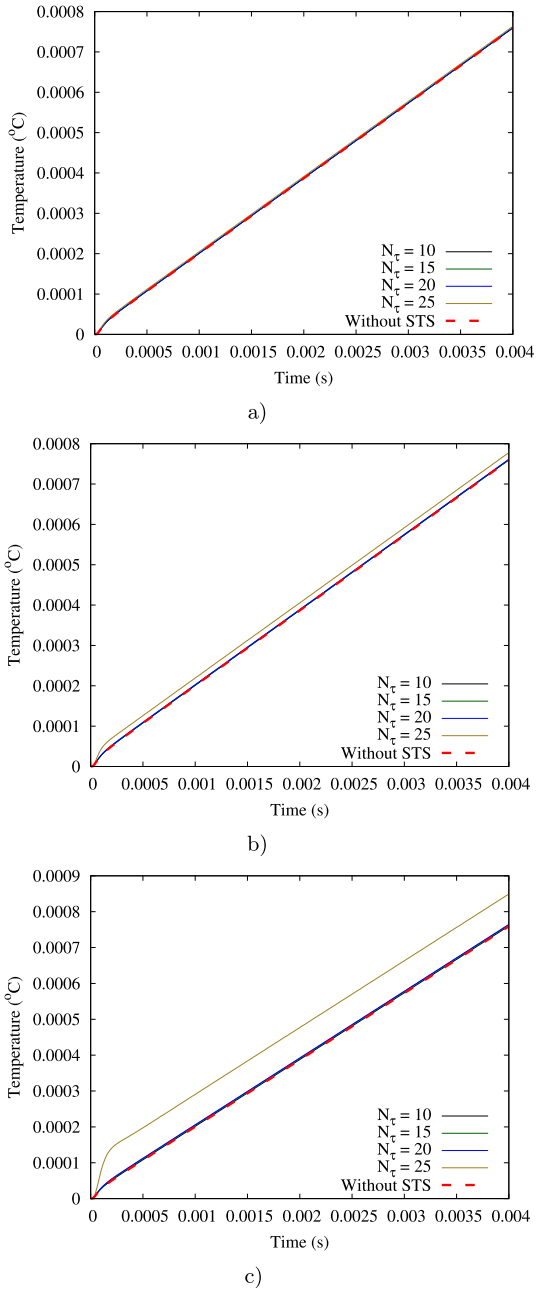

Fig. 20 Comparison of temperature evolution (at particle P, Fig. 9): **a** $\nu = 1\text{e}{-3}$, **b** $\nu = 1\text{e}{-4}$, **c** $\nu = 1\text{e}{-5}$

evaluated. Adiabatic boundary conditions (zero temperature gradient) were applied for the whole sample as shown in Fig. 15b. Zero initial conditions were assumed for the electric and thermal problems, for electric potential and temperature, respectively. The thermal model parameters specified in Sect. 9.1 were complemented with the following data for the electric model:

– specific electrical capacitance $c^{\text{el}} = 2 \times 10^6$ F/kg,
– electric conductivity $\kappa^{\text{el}} = 9.8 \times 10^5$ S/m,

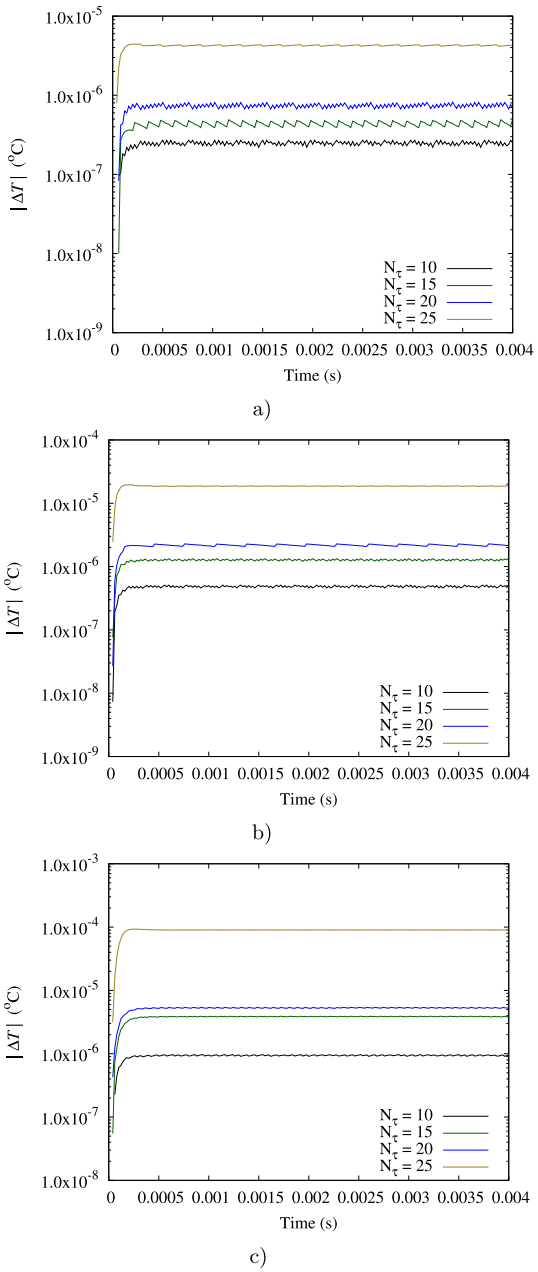

Fig. 21 Error in temperature evolution (at particle P, Fig. 9): **a** $\nu = 1$ e−3, **b** $\nu = 1$e−4, **c** $\nu = 1$e−5

- thickness of the grain boundary $\delta_{\mathrm{gb}} = 0.23\,\mu m$,
- conductivity-reduction factor for the grain boundary $\epsilon = 0.16$,
- safety factor for assessment of the critical time step $\alpha = 0.15$.

The parameters defining grain boundary resistance, ϵ and δ_{gb}, were calibrated in [21].

A similar thermo-electric problems were analysed in detail in [53] using the standard explicit forward Euler method for time integration. Here, we will investigate the performance and applicability of the STS scheme for the coupled problem. The STS simulations were performed for different combinations of STS parameters $N_\tau \in \{10, 15, 20, 25\}$ and $\nu \in \{1\mathrm{e}{-5},\ 1\mathrm{e}{-4},\ 1\mathrm{e}{-3}\}$. The ratio $\lambda^{\mathrm{el}}_{\min}/\lambda^{\mathrm{el}}_{\max}$ based on the minimum and maximum eigenvalues, estimated for the electric problem in Appendix 3, is $1.34\mathrm{e}{-4}$. This value is close to the ratio evaluated for the thermal problem, $1.275\mathrm{e}{-4}$. Two of the tested values of ν, $1\mathrm{e}{-5}$ and $1\mathrm{e}{-4}$, are in the interval $(0, \lambda_{\min}/\lambda_{\max})$ for both thermal and electric problems. The third value, $1\mathrm{e}{-3}$, is higher than the upper limit for both problems. Efficiency and accuracy of the STS scheme for different combinations of the STS parameters will be investigated by comparison to standard explicit solution.

The critical time steps, evaluated in Appendix, for the thermal and electric problems are $5.0881\mathrm{e}{-8}\,\mathrm{s}$ and $1.5345\mathrm{e}{-8}\,\mathrm{s}$, respectively. Therefore time integration step of the coupled problem is limited by the critical step of the electric problem, which is smaller of the two.

Figures 16 and 17 show the evolution of the distribution of the electric potential and temperature, respectively. Figure 16 shows the changes of the distribution of the electric potential in the transient phase until the steady-state distribution (Fig. 16d) is obtained. Figure 17 shows a uniform temperature distribution during heating due to the Joule effect. It was shown in [53] that despite nonuniform Joule heating at the particle scale, the temperature in the sample is uniform due to a high diffusivity of the metallic material.

Figure 18 presents the evolution of the electric potential at particle P at the half of the sample height (Fig. 9) for different combinations of STS parameters and the standard explicit solution. All the solutions present a fast increase in a short initial phase and a constant value at the steady-state phase. The curves in Fig. 18 obtained with various values of N_τ and $\nu = 1\mathrm{e}{-3}$ coincide nearly perfectly.

Errors in the solution of potential evolution V are analysed in analogy with the temperature evolution T in thermal problem in Sect. 9.1 Difference between STS solutions V_{STS} and standard explicit solution $V_{\mathrm{st-sxpl}}$ in the transient phase are plotted as absolute error $|\Delta V(t)|$ in Fig. 19a, c, e, and g. A rapid decrease in error can be seen for all cases. Assuming that the errors drop exponentially, the curves can be fitted according to Eq. (43). Exponential decay appears as a straight line when plotted on a semi-log scale as given by Eq. (44). Figure 19b, d, f, and h presents log-transformed absolute errors $\log_{10}|\Delta V(t)|$ plotted against time. The plots indicate quite good linear fitting with coefficient of determination R^2 generally higher 0.77, cf. Table 3. The error decay k can be evaluated from the slope of the linearly fitted lines according to the relation given in Eq. (46). The decay rates obtained for all parameter combinations are given in Table 3. For most cases, k has similar values. The only noticeable

Table 4 Performance metrics for the simulations of the thermoelectric problem with different combinations of STS parameters

STS parameters		Total No. of STS substeps	Total CPU time (s)	CPU time (s) of time stepping	Speedup (total CPU time)	Speedup (time stepping)
ν	N_τ					
0	1	1374238	39190	39166.5	1.00	1.00
1e−3	10	155090	4545	4536.0	8.62	8.63
	15	117450	3460	3452.0	11.33	11.35
	20	101860	2922	2913.2	13.41	13.44
	25	94500	2798	2789.9	14.01	14.04
1e−4	10	139110	4017	4007.8	9.76	9.77
	15	94260	2737	2729.3	14.32	14.35
	20	72280	2138	2129.7	18.33	18.39
	25	59425	1736	1728.2	22.58	22.66
1e−5	10	137470	4017	4007.8	9.76	9.77
	15	91800	2648	2640.6	14.80	14.83
	20	69020	2006	1998.4	19.54	19.60
	25	55375	1624	1615.7	24.13	24.24

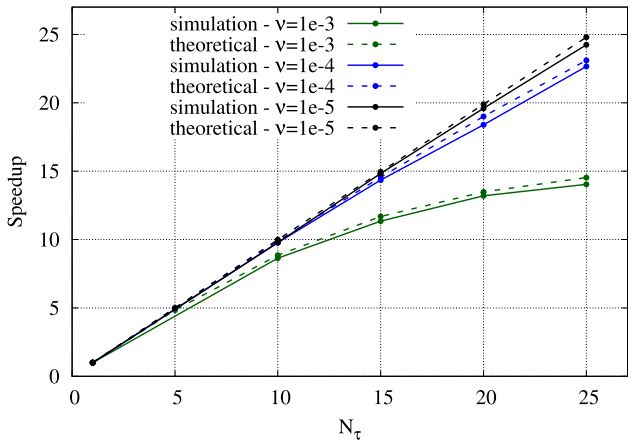

Fig. 22 Comparison of theoretical speedup and that achieved from thermo-electric simulations (CPU time of time stepping only)

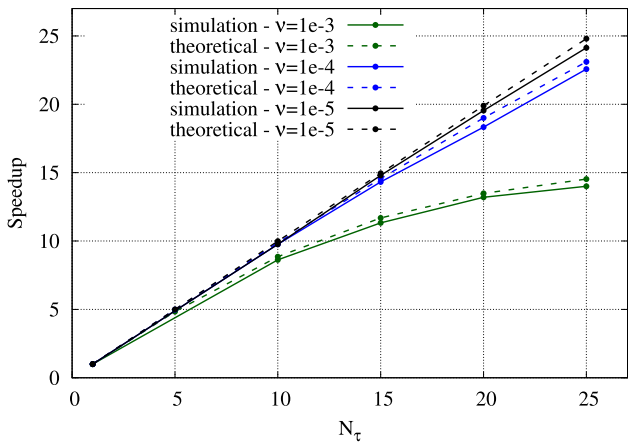

Fig. 23 Comparison of theoretical speedup and that achieved from thermo-electric simulations (total CPU time)

exception is the cases with N_τ= 25 and ν= 1e−5 where the decay rate is visibly slower. The exponential fits according to the Eqs. (43) with the decay constant k and the intercept Z taken from Eq. (44) are plotted in Fig. 19a, c, e, and g. To analyse the error quantitatively, mean absolute error (ΔV_{mean}) was evaluated using Eq. (47) where temperature T can be replaced by potential V. ΔV_{mean} values given in Table 3 show an overall increase with the increasing number of STS substeps N_τ. The increasing trend in error with the increase of N_τ can be seen for all the values of ν; though, it is more prominent for smaller ν (ν = 1e−4, 1e−5). This analysis shows that high values of N_τ in combination with small values of ν should be avoided to ensure accuracy of the STS solution.

Figure 20 presents temperature evolution at the at particle P at the half of the sample height (Fig. 9) for different combinations of STS parameters and the standard explicit solution. The temperature evolution is related to the electric current changes. In the initial short phase, corresponding to the transient phase in the electric problem, temperature increases nonlinearly. After the steady state is achieved in the electric problem the Joule heating is constant and the rate of increase in temperature is constant, therefore, the temperature increases linearly in time.

All the curves in Fig. 20, except for that corresponding to the highest value of N_τ ($N_\tau = 25$), overlap very well and are very close to the reference solution with the standard explicit time integration. The difference between STS and standard explicit solutions can be treated as error in STS solution. The errors are presented in semi-log plots in Fig. 21. It can be seen that the smaller N_τ and larger (but still small) ν are, the smaller the error is. The error increases in the initial phase and then stays constant. The error in temperature is affected by the error in the STS solution of the electric problem. Joule heating is proportional to the square of the electric potential. Therefore, the error in

temperature is proportional to the square of the error in the electric solution. This explains why we observe the largest difference for $N_\tau = 25$, for which the error is the largest. As was commented earlier, the error in the electric solution for the steady state becomes close to zero, and the difference in temperature is kept at the same level in the phase of the steady state in the electric problem.

Similarly to the thermal simulations, we analysed an increase in the computational efficiency yielded by the STS scheme compared to the standard forward Euler explicit time integration. Performance metrics obtained in the simulations for various combinations of the STS parameters are given in Table 4. Data for $\nu = 0$ and $N_\tau = 1$ represent the performance of the standard explicit scheme. The CPU time is given for the total execution and for the execution of the time stepping only, without taking into account the time for input of the data and initial calculations. Based on these CPU times and the respective CPU time of the standard explicit simulation, the speedups were calculated for the STS simulations with different combinations of N_τ and ν. The speedups are also presented graphically in Figs. 22 and 23 in comparison to the theoretical speedups. It can be seen that the speedups obtained in simulations are very close to the theoretical speedups. There is not much difference in the speedups for the whole execution and for the time stepping. In this case, the number of time steps is much higher than in the case of the thermal simulation (compare the data in Tables 2 and 4), so the CPU time for the data input and initial calculations is less significant. We can observe that the speedups can be obtained as high as 22.6 and 24.1 for $N_\tau = 25$ combined $\nu = 1\text{e}{-4}$ and $\nu = 1\text{e}{-5}$. However, the error analysis carried out above shows that the error in temperature for $N_\tau = 25$ may be unacceptably large. The STS scheme with $N_\tau = 20$ yields the speedups 18.33 ($\nu = 1$ e−4) and 19.54 ($\nu = 1\text{e}{-5}$) with much lower error, which usually can be acceptable in practice.

10 Conclusions

The super-stepping-acceleration method was implemented and validated for thermal, electric and thermoelectric discrete-element models. The implementation of the STS scheme in the framework of the DEM is very simple since it requires few changes to the standard solution algorithm. Numerical simulations have shown that the STS scheme gives a significant speedup with respect to the standard explicit forward Euler method. The runtime improvement is gained thanks to a reduction in the number of time steps. The speedup and accuracy depend on the length of the superstep, which in turn depends on the value of STS parameters, the number of substeps N_τ and parameter ν. The smaller the ν and the larger N_τ are, the larger the length of the superstep and speedup are. However, the errors are larger with the increase in the length of the superstep. Thus, the efficiency is a tradeoff against the accuracy. Higher speedups are obtained at the cost of an increase in errors. The values of the STS parameters should be chosen so that the speedup is as high as possible with acceptable errors. Numerical investigations performed in this work have shown that $N_\tau = 10$ –20 combined with $\nu = 1\text{e}{-4}$–$1\text{e}{-3}$ give the speedups as high as 15 and the solutions with acceptable errors.

The results of the performance studies show that the STS acceleration scheme gives a considerable improvement in the explicit integration of the first-order differential equations, and it can be successfully applied in the DEM framework for transient thermal, electric and thermo-electric analyses.

The present work is limited to the DEM simulations on the fixed particle configurations, and it can be used in problems in which the dynamic effects can be neglected. Coupling with the dynamics will be the subject of further investigation.

Appendix: Eigenvalue estimation

The formulation of the STS algorithm developed by Alexiades [35] and used in this work, employs the parameter ν satisfying inequality (25) that involves the minimum and maximum eigenvalues of the discrete system, $\lambda_{\min}$ and $\lambda_{\max}$, respectively. Since the global matrix is not built in the numerical implementation of the solution algorithm, the spectral bounds for the thermal problem are estimated below using computationally efficient approximations, rather than by explicitly solving a global eigenvalue problem.

A.1 Estimation of eigenvalues for thermal problem

Estimation of the maximum eigenvalue

The largest eigenvalue $\lambda^{\text{th}}_{\max}$ will be estimated taking advantage of its direct relationship to the critical time step of the explicit forward Euler scheme given by Eq. (21). In the numerical simulation of the thermal problem, the integration time step Δt_{cr} was assessed by taking the minimum of the critical time steps for two-particle systems

$$\min(\Delta t^{\text{cr}}_{ij}) = 7.1663\text{e}{-8}\,\text{s}$$

and multiplying it by a safety factor $\alpha = 0.3$ as given in Eq. (27)

$$\Delta t_{\mathrm{cr}} = 0.3 \cdot 7.1663\mathrm{e}{-8}\,\mathrm{s} = 2.1499\mathrm{e}{-8}\mathrm{s}.$$

For the evaluation of $\lambda_{\max}^{\mathrm{th}}$, we determined the actual critical time finding the maximum value of α giving the stable solution. We performed simulations for $0.3 < \alpha < 1$. We obtained the stability limit using the bisection method—we were iteratively halving the interval and checking the stability of the solution in the midpoint. Unstable solution was signalled by a sudden and rapid/sudden increase of temperature to unrealistic values (explosion of the solution). In this way, the limiting value for stability $\alpha^* \approx 0.71$ was found. Thus, the actual critical time step was determined as

$$\Delta t_{\mathrm{cr}}^{*} = 0.71 \cdot 7.1663\mathrm{e}{-8}\,\mathrm{s} = 5.0881\mathrm{e}{-8}\,\mathrm{s}.$$

Accordingly, the maximum eigenvalue is estimated as:

$$\lambda_{\max}^{\mathrm{th}} = \frac{2}{\Delta t_{\mathrm{cr}}^{*}} = \frac{2}{5.0881\mathrm{e}{-8}\,\mathrm{s}} = 3.93074\mathrm{e}7\mathrm{s}^{-1}.$$

Estimation of the minimum eigenvalue

The smallest eigenvalue $\lambda_{\min}^{\mathrm{th}}$ of the discrete system will be assessed using the analytical solution of the eigenvalue problem corresponding to the continuous heat conduction equation equivalent to the analysed discrete problem. The thermal problem analysed in Sect. 9.1 can be idealised as a one-dimensional heat conduction problem along the *z*-axis. Due to the uniform prescribed temperatures at the top and bottom and insulated lateral boundaries heat in the radial direction can be neglected, and temperatures at sample cross-sections are approximately uniform. Therefore the analysed problem can be described approximately by the differential equation

$$\frac{\partial T(z,t)}{\partial t} = D\frac{\partial^2 T(z,t)}{\partial z^2} \tag{48}$$

with Dirichlet boundary conditions

$$T(0,t) = T_{\mathrm{bottom}} = 0^{\circ}\mathrm{C}\,, \quad T(L,t) = T_{\mathrm{top}} = 10^{\circ}\mathrm{C}\,, \tag{49}$$

where L, the height of the DEM sample, is the length of the computational domain, and D^{th} is an effective thermal diffusivity evaluated as:

$$D^{\mathrm{th}} = \frac{\kappa_{\mathrm{eff}}^{\mathrm{th}}}{\rho_{\mathrm{b}} c^{\mathrm{th}}}\,. \tag{50}$$

Assuming a solution of Eq. (48) in the form

$$T(z,t) = \phi(z)\mathrm{e}^{-\lambda D^{\mathrm{th}} t}\,, \tag{51}$$

where $\phi(z)$ satisfies the boundary conditions (49), we obtain a spatial eigenvalue problem

$$-\frac{\partial^2 \phi}{\partial z^2} = \lambda\phi\,. \tag{52}$$

with λ being the eigenvalue and ϕ—the corresponding eigenfunction. Solution of the eigenvalue problem (52) yields the eigenvalues in the form [60, 61]:

$$\lambda_n = \frac{n^2\pi^2 D^{\mathrm{th}}}{L^2}\,. \tag{53}$$

The smallest eigenvalue is that corresponding to $n = 1$

$$\lambda_{\min}^{\mathrm{th}} = \lambda_1 = \frac{\pi^2 D^{\mathrm{th}}}{L^2}\,. \tag{54}$$

Calculations defined by Eqs. (50) and (54) have been carried out taking parameters given in Sect. 9.1, specific heat capacity $c^{\mathrm{th}} = 640\ \mathrm{J/(kg\,K)}$ and the sample height $L = 166\,\mu m$, as well as effective properties determined in our previous work [28], effective thermal conductivity $\kappa_{\mathrm{eff}}^{\mathrm{th}} = 41.5\ \mathrm{W/(m\,K)}$ and bulk density $\rho_{\mathrm{b}} = 4633.44\ \mathrm{kg\,m^{-3}}$. Using these data in Eqs. (50) and (54) we obtain the effective diffusivity $D^{\mathrm{th}} = 1.399\mathrm{e}{-5}\ \ \mathrm{m^2 s^{-1}}$

and the minimum eigenvalue

$$\lambda_{\min}^{\mathrm{th}} = 5.0124e3\ \mathrm{s}^{-1}\,.$$

Hence the eigenvalue ratio is given as:

$$\frac{\lambda_{\min}^{\mathrm{th}}}{\lambda_{\max}^{\mathrm{th}}} \approx 1.275\mathrm{e}{-4}.$$

A.2 Estimation of eigenvalues for electrical problem

Taking advantage of the mathematical analogy between thermal and electrical problem, we evaluate the eigenvalues in the electrical problem in the same way as it was done above for the thermal problem.

Estimation of the maximum eigenvalue

Maximum eigenvalue $\lambda_{\max}^{\mathrm{el}}$ is estimated using its relationship to the critical time step of the explicit forward Euler scheme given by Eq. (21). In the electrical problem, the minimum of the critical time steps for two-particle systems was determined as

$$\min(\Delta t_{ij}^{\mathrm{cr}}) = 1.9424\mathrm{e}{-8}\,\mathrm{s}.$$

The limiting value for stability of $\alpha^* \approx 0.79$ was found iteratively by the bisection method. The actual critical time step was determined as

$$\Delta t^*_{\mathrm{cr}} = 0.79 \cdot 1.9424\mathrm{e}{-8}\,\mathrm{s} = 1.5345\mathrm{e}{-8}\,\mathrm{s}.$$

Accordingly, the maximum eigenvalue is estimated as:

$$\lambda^{\mathrm{el}}_{\max} = \frac{2}{\Delta t^*_{\mathrm{cr}}} = \frac{2}{1.5345\mathrm{e}{-8}\,\mathrm{s}} = 1.3034\mathrm{e}8\,\mathrm{s}^{-1}.$$

Estimation of the minimum eigenvalue

The smallest eigenvalue $\lambda^{\mathrm{el}}_{\min}$ for the electrical problem will be estimated using the analogy between thermal and electrical problem. Analytical solution of one-dimensional heat conduction problem presented in Appendix A.1 can be translated to an electrical problem yielding the solution of the minimum eigenvalue problem in the form:

$$\lambda^{\mathrm{el}}_{\min} = \frac{\pi^2 D^{\mathrm{el}}}{L^2}, \tag{55}$$

where L, the height of the DEM sample, is the length of the computational domain, and D^{el} is an effective electrical diffusivity (analogous to thermal diffusivity, cf. [62]) evaluated as:

$$D^{\mathrm{el}} = \frac{\kappa^{\mathrm{el}}_{\mathrm{eff}}}{\rho_{\mathrm{b}} c^{\mathrm{el}}}. \tag{56}$$

Calculations defined by Eqs. (56) and (55) have been carried out taking parameters given in Sect. 9.2, specific electric capacity $c = 2e6\ \mathrm{F/kg})$ and the sample height $L = 166\,\mu m$, as well as effective properties determined in our previous work [21], effective electrical conductivity $\kappa^{\mathrm{el}}_{\mathrm{eff}} = 4.518\mathrm{e}5\ \mathrm{S/m}$ and bulk density $\rho_{\mathrm{b}} = 4633.44\ \mathrm{kg\,m^{-3}}$. Using these values, we obtain the effective diffusivity $D^{\mathrm{el}} = 4.875\mathrm{e}{-5}\ \ \mathrm{m^2 s^{-1}}$ and the minimum eigenvalue

$$\lambda^{\mathrm{el}}_{\min} = 1.746e4\ \mathrm{s}^{-1}.$$

Hence the eigenvalue ratio is given as:

$$\frac{\lambda^{\mathrm{el}}_{\min}}{\lambda^{\mathrm{el}}_{\max}} \approx 1.34\mathrm{e}{-4}.$$

Acknowledgements Jerzy Rojek thanks Dr Martin Dutko for useful discussions and kind hospitality while visiting Rockfield, Swansea, UK.

Author contributions J.R. and F.N. wrote the manuscript text. All authors reviewed the manuscript. J.R. implemented algorithm in the numerical program, and F.N. performed numerical simulations and analyzed the results.

Funding This work was supported by National Science Centre, Poland (Grant number: 2019/35/B/ST8/03158). Jerzy Rojek acknowledges partial financial support from the EU through the EffectFact project (No. 101008140) funded within the H2020-MSCA-RISE-2020 programme.The project EffectFact was co-financed by the Polish Ministry of Science and Higher Education under the program entitled International Co-financed Projects.

Data availability No datasets were generated or analysed during the current study.

Declarations

Conflict of interest This work was supported by National Science Centre, Poland (Grant number: 2019/35/B/ST8/03158) Jerzy Rojek acknowledges partial financial support from the EU through the EffectFact project (No. 101008140) funded within the H2020-MSCA-RISE-2020 programme.

References

1. Melka, S., Bézian, J.-J.: L'isolation thermique par les matériaux granulaires. Revue Générale de Thermique **36**, 345–353 (1997)
2. Tolochko, N.K., Arshinov, M.K., Gusarov, A.V., Titov, V.I., Laoui, T., Froyen, L.: Mechanisms of selective laser sintering and heat transfer in Ti powder. Rapid Prototyping Journal **9**, 314–326 (2003)
3. Polesek-Karczewska, S., Kardaś, D.: Issues on numerical modelling of transport processes in granular reactive media—an approach with thermal relaxation. Archives of Thermodynamics **45**, 5–12 (2024)
4. Chen, J.C., Grace, J.R., Golriz, M.R.: Heat transfer in fluidized beds: design methods. Powder Technol. **150**, 123–132 (2005)
5. Ott, J., Völker, B., Gan, Y., McMeeking, R.M., Kamlah, M.: A micromechanical model for effective conductivity in granular electrode structures. Acta. Mech. Sin. **29**, 682–698 (2013)
6. Abeles, B., Sheng, P., Coutts, M.D., Arie, Y.: Structural and electrical properties of granular metal films. Adv. Phys. **24**, 407–461 (1975)
7. Zhai, C., Hanaor, D., Proust, G., Gan, Y.: Electrical transport in granular metals. EPJ Web Conf. **140**, 05010 (2017)
8. Stassi, S., Cauda, V., Canavese, G., Pirri, C.F.: Flexible tactile sensing based on piezoresistive composites: A review, 3 (2014)
9. Glatz, A., Beloborodov, I.S.: Thermoelectric properties of granular metals. Phys. Rev. B **79**, 041404(R) (2009)

10. Mechanisms, M., Developments, T.: O. Guillon, J. Gonzalez-Julian, B. Dargatz, T. Kessel, G. Schierning, J. R ä thel, and M. Herrmann. Field-Assisted Sintering Technology/Spark Plasma Sintering. Adv. Eng. Mater. **16**, 830–849 (2014)
11. Morimoto, T., O'Sullivan, C., Taborda, D.M.G.: Exploiting DEM to link thermal conduction and elastic stiffness in granular materials. J. Eng. Mech. **148**, 04021139 (2022)
12. Schneider, L.C.R., Martin, C.L., Bultel, Y., Bouvard, D., Siebert, E.: Discrete modelling of the electrochemical performance of SOFC electrodes. Electrochim. Acta **52**, 314–324 (2006)
13. Cundall, P.A., Strack, O.D.L.: A discrete numerical method for granular assemblies. Geotechnique **29**, 47–65 (1979)
14. Bardet, J.P., Proubet, J.: Application of micromechanics to incrementally nonlinear constitutive equations for granular media. In: Biarez, J., Gourves, R. (eds.) Powders and Grains. Proceedings of the International Conference on Micromechanics of Granular Media, Clermont-Ferrand, 4–8 September 1989, pp. 265–270. Balkema, Rotterdam (1989)
15. Potyondy, D.O., Cundall, P.A.: A bonded-particle model for rock. Int. J. Rock Mech. Min. Sci. **41**, 1329–1364 (2004)
16. Huang, H.: Discrete Element Modeling of Tool-Rock Interaction. PhD thesis, University of Minnesota, (1999)
17. Rojek, J., Oñate, E., Labra, C., Kargl, H.: Discrete element simulation of rock cutting. Int. J. Rock Mech. Min. Sci. **48**(6), 996–1010 (2011)
18. Feng, Y.T., Han, K., Owen, D.R.J.: Discrete thermal element modelling of heat conduction in particle systems: Pipe-network model and transient analysis. Powder Technol. **193**, 248–256 (2009)
19. Rojek, J.: Discrete element thermomechanical modelling of rock cutting with valuation of tool wear. Computational Particle Mechanics **1**, 71–84 (2014)
20. Zohdi, T.: A direct particle-based computational framework for electrically enhanced thermo-mechanical sintering of powdered materials. Math. Mech. Solids **19**, 93–113 (2014)
21. Nisar, F., Rojek, J., Nosewicz, S., Szczepański, J., Kaszyca, K., Chmielewski, M.: Discrete element model for effective electrical conductivity of spark plasma sintered porous materials. Computational Particle Mechanics **11**, 2191–2201 (2024)
22. Zhang, H.W., Zhou, Q., Zheng, Y.G.: A multi-scale method for thermal conduction simulation in granular materials. Comput. Mater. Sci. **50**, 2750–2758 (2011)
23. Zohdi, T.I.: A computational framework for agglomeration in thermochemically reacting granular flows. Proceedings of the Royal Society A: Mathematical, Physical and Engineering Sciences **460**, 3421–3445 (2004)
24. Terreros, I., Iordanoff, I., Charles, J.L., Coupard, D., Tchernaieff, S.: Discrete Element Method, a tool to investigate complex thermo mechanical behaviour: Application to friction stir welding. Int.J. Mater. Form. **2**, 573–576 (2009)
25. Nguyen, V.D., Fortin, J., Guessasma, M., Bellenger, E., Cogné, C.: Thermomechanical modelling of friction effects in granular flows using the discrete element method. J. Mech. Mater. Struct. **4**, 413–426 (2009)
26. Quintana-Ruiz, O.D., Campello, M.B.: A thermo-mechanical formulation for the modeling of discrete particle systems. In: Proceedings of the XL Ibero-Latin-American Congress on Computational Methods in Engineering, ABMEC, Natal/RN, Brazil, November 11-14, (2019)
27. Paiva Teixeira, M.H., Skorych, V., Janssen, R., Gomez Gonzalez, S.Y., De Noni Jr, A., Rodrigues Neto, J.B., Hotza, D., Dosta, M.: High heating rate sintering and microstructural evolution assessment using the discrete element method. Open Ceramics **8**, 100182 (2021)
28. Nisar, F., Rojek, J., Nosewicz, S., Kaszyca, K., Chmielewski, M.: Evaluation of effective thermal conductivity of sintered porous materials using an improved discrete element model. Powder Technol. **437**, 3 (2024)
29. Jung, D.W.: Study of dynamic explicit analysis in sheet metal forming processes using faster punch velocity and mass scaling scheme. J. Mater. Eng. Perform. **7**, 479–490 (1998)
30. Shi, Y., Ding, S., Qiu, T., Liu, C., Zhang, S.: Bi-Fo time scaling method in the numerical simulation of transient conjugate heat transfer. Propulsion and Power Research **10**, 209–223 (2021)
31. Oñate, E., de Pouplana, I., Zarate, F.: Explicit time integration scheme with large time steps for first order transient problems using finite increment calculus. Comput. Methods Appl. Mech. Eng. **402**, 115332 (2022)
32. Gentzsch, W.: Numerical solution of linear and non-linear parabolic differential equations by a time-discretisation of third order accuracy. In Ernst Heinrich Hirschel, editor, *Proceedings of the Third GAMM-Conference on Numerical Methods in Fluid Mechanics*, pages 109–117. Friedr. Vieweg & Sohn Verlagsgesellschaft mbH, Braunschweig 1980, 10 (1979)
33. Droux, J.-J.: Three-dimensional numerical simulation of solidification by an improved explicit scheme. Comput. Methods Appl. Mech. Eng. **85**, 57–74 (1991)
34. Alexiades, V.: Super-time-stepping acceleration of explicit schemes for phase-change problems. IMACS'94 **2**, 533–536 (1994)
35. Alexiades, V., Amiez, G., Gremaud, P.-A.: Super-time-stepping acceleration of explicit schemes for parabolic problems. Commun. Numer. Methods Eng. **12**, 31–42 (1996)
36. Lewis, R.W., Masters, I., Cross, J.T.: Automatic timestep selection for the super-time-stepping acceleration on unstructured grids using object-oriented programming. Commun. Numer. Methods Eng. **13**, 249–260 (1997)
37. Gurski, K.F., O'Sullivan, S.: An explicit super-time-stepping scheme for non-symmetric parabolic problems. AIP Conf. Proc. **1281**, 761–764 (2010)
38. Gurski, K., O'Sullivan, S.: A stability study of a new explicit numerical scheme for a system of differential equations with a large skew-symmetric component. SIAM J. Numer. Anal. **49**, 368–386 (2011)
39. Pelovska, G.: An improved explicit scheme for age-dependent population models with spatial diffusion. Int. J. Numer. Anal. Model. **5**, 466–490 (2008)
40. Barnaś, D., Bieniasz, L.K.: Utility of super-time-stepping for electroanalytical digital simulations by explicit finite difference methods. Part 1: Spatially one-dimensional models. J. Electroanal. Chem. **815**, 210–219 (2018)
41. Barnaś, D., Bieniasz, L.K.: Utility of super-time-stepping for electroanalytical digital simulations by explicit finite difference methods. Part 2: Spatially two- and three-dimensional models. J. Electroanal. Chem. **838**, 204–211 (2019)
42. Oñate, E., Zarate, F., Gimenez, J.M., Lohner, R., Idelsohn, S.R.: Fast explicit time integration schemes for parabolic problems in mechanics. Int. J. Numer. Meth. Eng. **125**, e7477 (2024)
43. Moscardini, M., Gan, Y., Pupeschi, S., Kamlah, M.: Discrete element method for effective thermal conductivity of packed pebbles accounting for the smoluchowski effect. Fusion Eng. Des. **127**, 192–201 (2018)
44. Gaviño, D., Cortés, E., García, J., Calderón-Vásquez, I., Cardemil, J., Estay, D., Barraza, R.: A discrete element approach to model packed bed thermal storage. Appl. Energy **325**, 11 (2022)
45. Chen, L., Wang, C., Moscardini, M., Kamlah, M., Liu, S.: A dem-based heat transfer model for the evaluation of effective thermal conductivity of packed beds filled with stagnant fluid: Thermal contact theory and numerical simulation. Int. J. Heat Mass Transf. **132**, 331–346 (2019)
46. Cheng, G.J., Yu, A.B.: Particle scale evaluation of the effective thermal conductivity from the structure of a packed bed:

Radiation heat transfer. Ind. Eng. Chem. Res. **52**, 12202–12211 (2013)
47. Haddad, H., Leclerc, W., Alhajj Hassan, G., Ammar, A., Pélegris, C., Guessasma, M., Bellenger, E.: Numerical investigation of heat conduction in heterogeneous media with a discrete element method approach. Int. J. Therm. Sci. **164**, 106799 (2021)
48. Peng, Z., Doroodchi, E., Moghtaderi, B.: Heat transfer modelling in Discrete Element Method (DEM)-based simulations of thermal processes: Theory and model development. Prog. Energy Combust. Sci. **79**, 100847 (2020)
49. Bergman, T.L., Lavine, A.S., Incropera, F.P., Dewitt, D.P.: Fundamentals of Heat and Mass Transfer, 7th edn. John Wiley & Sons, USA (2011)
50. Weedy, B.M.: The analogy between thermal and electrical quantities. Electric Power Systems Research **15**, 197–201 (1988)
51. González-Morales, P.A., Khomenko, E., Downes, T.P., De Vicente, A.: MHDSTS: A new explicit numerical scheme for simulations of partially ionised solar plasma. Astron. Astrophys. **615**, 7 (2018)
52. French, L.: Super-time-stepping for advection-diffusion. Master's thesis, University of Tennessee, Knoxville, 5 (1997)
53. Nisar, F., Rojek, J., Nosewicz, S., Kaszyca, K., Chmielewski, M.: Coupled thermo-electric discrete element model for spark plasma sintering. Powder Technol. **458**, 120957 (2025)
54. Rojek, J., Kasztelan, R., Tharmaraj, R.: Discrete element thermal conductance model for sintered particles. Powder Technol. **405**, 117521 (2022)
55. Martin, C.L., Schneider, L.C.R., Olmos, L., Bouvard, D.: Discrete element modeling of metallic powder sintering. Scripta Mater. **55**, 425–428 (2006)
56. Olmos, L., Martin, C.L., Bouvard, D.: Sintering of mixtures of powders: Experiments and modelling. Powder Technol. **190**, 134–140 (2009)
57. Larsson, P.-L., Biwa, S., Storakers, B.: Analysis of cold and hot isostatic compaction of spherical particles. Acta Mater. **44**, 3655–3666 (1996)
58. Coble, R.L.: Initial sintering of alumina and hematite. Journal of American Ceramic Society **41**, 55–62 (1958)
59. Coble, R.L.: Effect of particle size distribution in initial-stage sintering. J. Am. Ceram. Soc. **56**, 461–466 (1973)
60. Goertzel, G., Tralli, N.: Goertzel, Gerald H and Tralli, Nunziobook- Some Mathematical Methods of Physics. McGraw-Hill Book Company Inc (1960)
61. Abdisa, L.T.: One dimensional heat equation and its solution by the methods of separation of variables, fourier series and fourier transform. Journal of Applied & Computational Mathematics **10**, 1–6 (2021)
62. Abd-Elhady, M.S., Ibrahim, M., Kandil, H.A., Ali, A.R.: "Electrical diffusivity" as a new transport property to categorize the diffusion of charge in materials. Discover Applied Sciences **7**, 10 (2025)